Mechanical testing and microstructural analysis of wire arc additively manufactured steels

Cheng Huang [a,*], Pinelopi Kyvelou [a], Ruizhi Zhang [a,*], T. Ben Britton [b], Leroy Gardner [a]

[a] Department of Civil and Environmental Engineering, Imperial College London, UK

[b] Department of Materials, Imperial College London, UK

[*]Corresponding author

Email address: cheng.huang118@imperial.ac.uk and r.zhang18@imperial.ac.uk

Abstract

Wire arc additive manufacturing (WAAM) is a metal 3D printing method that allows the cost-effective and efficient production of large-scale elements, and has thus gained great interest from architects and structural engineers. Integration of this novel technology into the construction industry, however, requires the development of a clear understanding of the mechanical behaviour of WAAM materials. To this end, a comprehensive experimental study into the mechanical properties and microstructure of WAAM plates made of normal- and high-strength steels has been undertaken and is reported herein. A total of 137 as-built and machined tensile coupons were tested, extracted in various directions relative to the print layer orientation from WAAM plates of two nominal thicknesses, built using different deposition strategies. The influence of the geometric undulations inherent to the WAAM process and deposition strategy on the resulting mechanical properties was investigated. Microstructural characterisation was also performed by means of optical microscopy (OM) and electron backscatter diffraction (EBSD). The WAAM normal-strength steel plates exhibited a principally ferritic-pearlitic microstructure, while the WAAM high-strength steel plates displayed a mixed microstructure featuring ferrite, bainite and martensite. The EBSD analysis revealed a weak crystallographic texture, which explained the observed mechanical properties being almost isotropic. No significant differences in tensile properties were observed with the different deposition strategies, except for some variation in ductility. The geometric undulations of the as-built coupons resulted in some reduction in effective mechanical properties and a degree of anisotropy. Overall, the examined WAAM material exhibited consistent mechanical properties, a Young's modulus comparable to conventionally-produced steel plates, marginally lower

strength, reflecting the slower cooling conditions than is customary, and good ductility.

Keywords: Carbon steel; High strength steel; Material anisotropy; Mechanical properties; Metal 3D printing; Microstructure; Tensile coupon tests; Wire arc additive manufacturing.

1 Introduction

Additive manufacturing (AM), commonly termed 3D printing, is a manufacturing process whereby objects are formed by the successive deposition of material in a layer-by-layer fashion [1]. AM is being increasingly employed across multiple industries due to several significant advantages over conventional fabrication techniques, including higher levels of automation, greater design freedom and reduced material consumption. The application of AM in civil engineering has also been recently explored [2–6]; in particular, the recent emergence of metal 3D printing within the construction sector has given rise to heightened interest among structural engineers and researchers [7–9].

Of the existing methods of metal 3D printing [1], wire arc additive manufacturing (WAAM) is considered to be the most suitable for the construction industry owing to its use of widely available welding technology and its ability to produce large elements in a relatively quick and economic fashion. Early uses of WAAM in construction include the stainless steel MX3D bridge spanning a canal in Amsterdam [8], a steel bridge spanning a stream in Darmstadt [10] and complex connection nodes [11]; all provide a glimpse of the potential of WAAM. There remain, however, a number of technical challenges associated with WAAM, many of which relate to uncertainties and variability in the mechanical and microstructural properties of WAAM materials, as addressed in the present study.

Previous studies in the mechanical properties of WAAM material have largely focused on stainless steels [12–14], titanium alloys [15,16], aluminium alloys [17,18] and other alloys [19,20]. More recently, WAAM carbon steels have increasingly become the subject of attention. Moderate mechanical anisotropy was observed in both WAAM normal- and high-strength steels by Sun et al. [21], Lin et al. [22] and Rodrigues et al. [23], although others [24–26] found the mechanical properties to be almost isotropic, with no pronounced crystallographic texture detected. Tensile tests were conducted on WAAM steel plates in [22,24,27], where the coupon extraction location was shown to influence the resulting mechanical properties. This influence was correlated with the local thermal history of the

WAAM plates [22]. Different deposition strategies, which can affect the heat evolution and geometric accuracy of WAAM parts, have also been explored [28,29].

Hitherto, the mechanical properties and microstructure of WAAM carbon steels have not been comprehensively characterised. To bridge this knowledge gap, a comprehensive series of tensile tests has been carried out on normal- and high-strength WAAM steel plates; the microstructure of both steel grades has also been examined. 3D laser scanning and digital image correlation (DIC) were employed in the testing program for the digital capture of the geometric properties and deformation responses of the WAAM coupons, respectively. The production, geometric measurements and mechanical testing of the WAAM coupons are described. Detailed insight into the geometric, mechanical and microstructural characteristics of the examined WAAM materials is provided.

2 Production and preparation of test specimens

2.1 Feedstock material and manufacturing process

Two types of feedstock wire — ER70S-6 (EN ISO 14341-A G 42 3 M21 3Si1) and ER110S-G (EN ISO 16834-A G 69 4 M21 Mn3Ni1CrMo) — were adopted for the additive manufacturing of the normal- and high-strength steel specimens, respectively. The chemical composition and mechanical properties of the as-welded feedstock material, as provided by the manufacturer, are reported in Tables 1 and 2, respectively. Printing of the specimens was undertaken by the Dutch company MX3D, using a 6-axis ABB robot equipped with a metal inert gas (MIG) welding system. In order to obtain planar WAAM elements, oval tubes (with flat sides) of 8 mm and 3 mm nominal thickness t_{nom} were built up on a substrate plate, in a series of successive layers of weld material; printing of typical oval tubes is illustrated in Fig. 1. During the WAAM process, the robot operated in repetitive loop-shaped paths (the start and end point of which was varied between layers), with a controlled travel speed, wire feed rate, arc voltage and current and dwell times; a summary of the key process parameters, as provided by the manufacturer, is given in Table 3.

Table 1 Chemical composition (in % by weight) of ER70S-6 and ER110S-G wires from the manufacturer's datasheet.

Feedstock wire	C	Si	Mn	Cr	Ni	Mo	Cu	V	Fe
ER70S-6	0.07	0.85	1.43	0.04	0.01	0.01	0.01	0.01	Balance
ER110S-G	0.09	0.54	1.60	0.27	1.37	0.25	1.37	0.08	Balance

Table 2 Mechanical properties (as-welded) of ER70S-6 and ER110S-G wires from the manufacturer's datasheet.

Feedstock wire	Yield strength (MPa)	Tensile strength (MPa)	Elongation (%)	Impact energy at -40°C (J)
ER70S-6	471	580	25	73
ER110S-G	735	799	18	55

Table 3 Process parameters used for WAAM plates.

Process parameters	Details	
	t_{nom} = 8 mm	t_{nom} = 3 mm
Feedstock wire	ER70S-6	ER70S-6/ER110S-G
Wire diameter (mm)	1.2	0.8
Travel speed (mm/s)	8	8
Wire feed rate (m/min)	4	3
Welding voltage (V)	24.8	14.8
Welding current (A)	130	54
Gas flow rate (L/min)	16	14
Welding mode	Pulsed welding	Short-arc welding
Shielding gas	82% Ar + 18% CO_2	82% Ar + 18% CO_2
Dwell time (s)	30	30

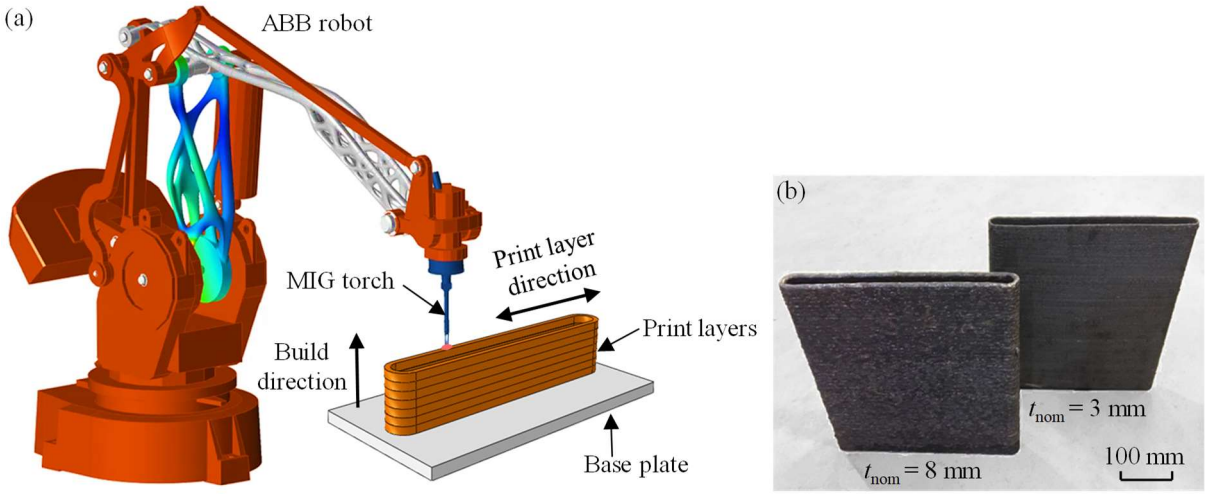


Fig. 1. Illustration of the WAAM process: (a) an oval tube being printed; (b) finished oval tubes of 8 mm and 3 mm nominal thickness.

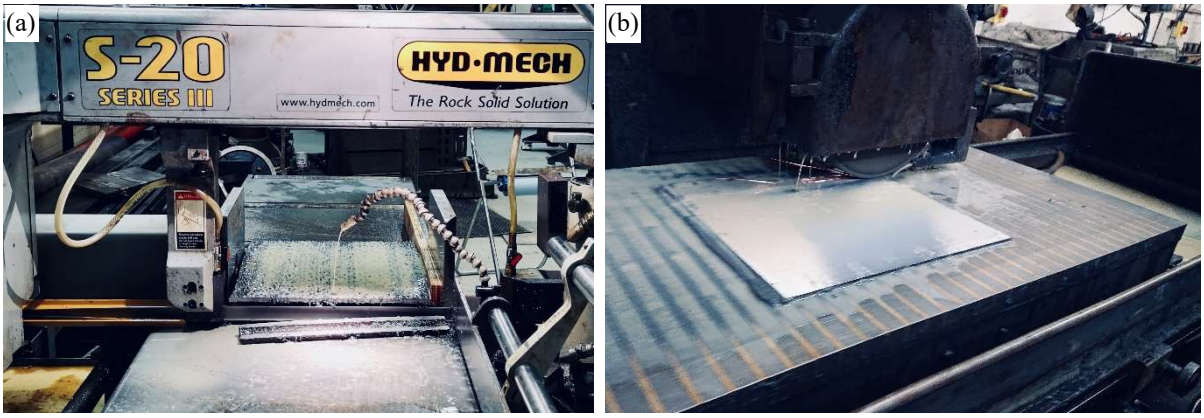


Fig. 2. (a) Cutting of an oval tube using a band saw; (b) milling a WAAM plate using a slitting saw.

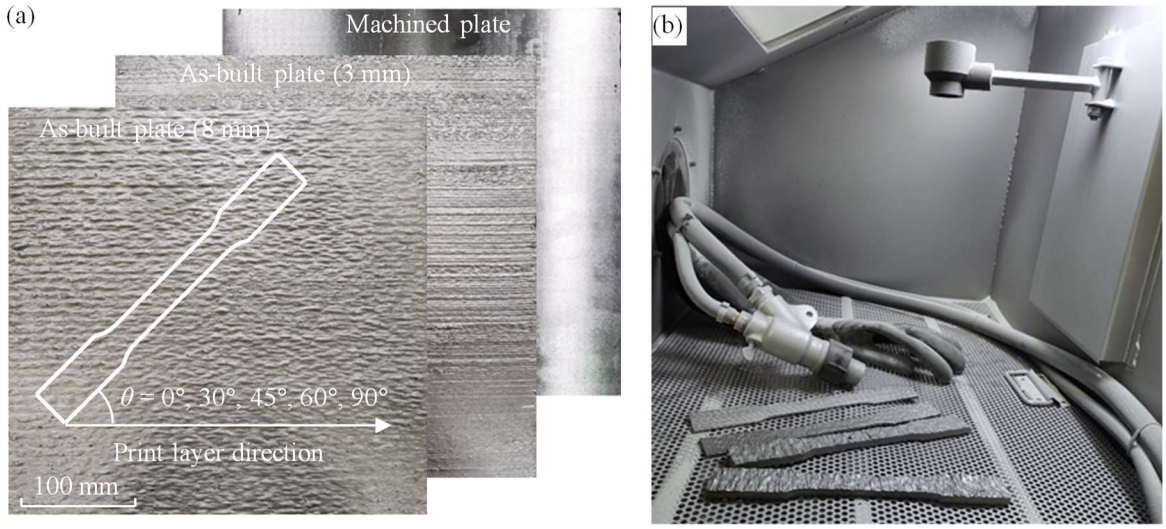


Fig. 3. (a) Typical as-built and machined WAAM plates and orientations of extracted tensile coupons; (b) sandblasting of typical coupons.

Upon completion of printing, the oval tubes were detached from the base plate using a plasma arc cutter, and flat plates were then extracted from the tubes using a band saw – see Fig. 2(a). WAAM plates have an inherently undulating geometry in their as-built condition. In order to assess the influence of the as-built geometry on the effective mechanical properties, a subset of the WAAM plates was milled flat using a slitting saw, as shown in Fig. 2 (b), enabling both as-built and machined coupons to be tested; the surfaces of typical as-built and machined plates are compared in Fig. 3(a).

A range of deposition strategies were employed in this study, realised by reversing deposition directions or introducing an elongated time interval between certain layers during fabrication, as defined in Table 4. Plate types A1 and A2 were built using the normal- and high-strength steel wires, respectively, both employing the default WAAM deposition strategy that was adopted for the construction of the MX3D bridge [8], in which the deposition direction was

reversed every layer. Plate types A3, A4 and A5 were all produced using the normal-strength steel wire. For plate type A3, the deposition direction was reversed every three layers. Plate type A4 was produced as per plate type A1, but an elongated pause was introduced at the mid-height of the plate, allowing it to cool down to ambient temperature, after which the second half of the plate was printed. For plate type A5, the same deposition direction was used throughout printing.

2.2 Specimen preparation

The tensile coupons were extracted from the as-built and machined plates by means of water jet cutting. The coupons were cut at various orientations (θ = 0°, 30°, 45°, 60°, 90°, as defined in Fig. 3) relative to the print layer direction, to investigate any potential material anisotropy. Following extraction from their parent plates, the as-built coupons were sandblasted with glass beads to remove any welding soot arising from the WAAM process, but had no further surface treatment; sandblasting of typical specimens is illustrated in Fig. 3(b). Fig. 4 shows typical sandblasted coupons extracted in various orientations, where the coupon dimensions, determined in accordance with EN ISO 6892-1 [30], are also presented.

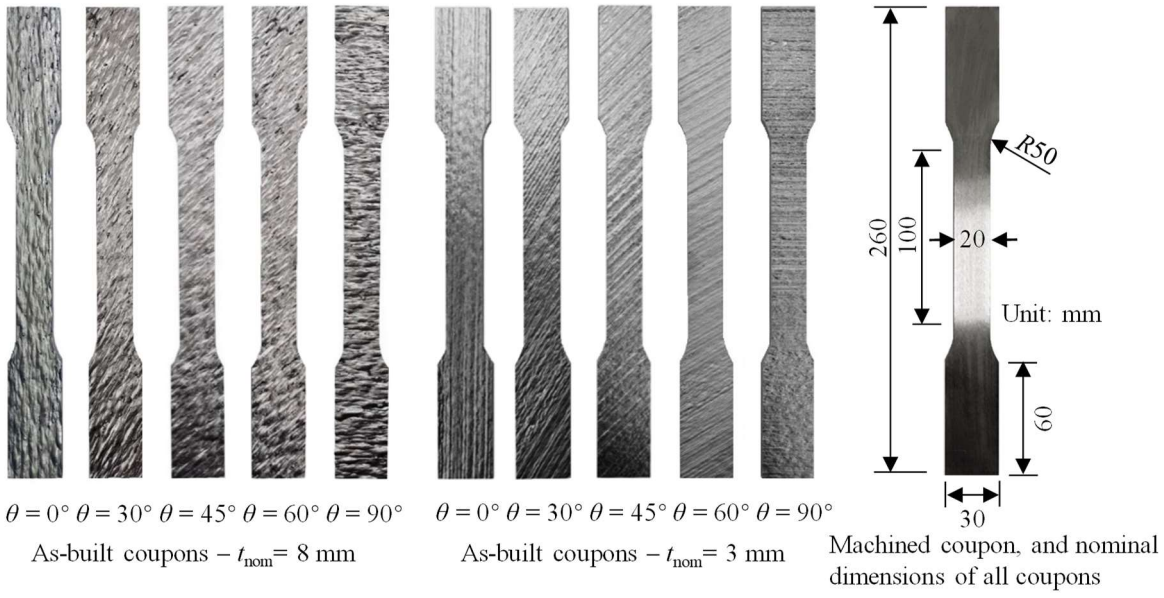
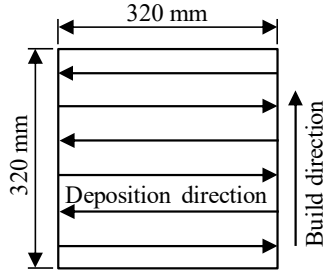
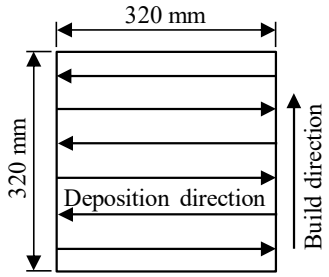
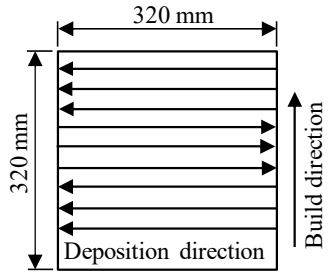
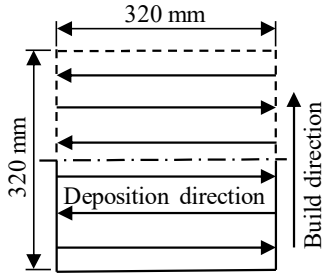
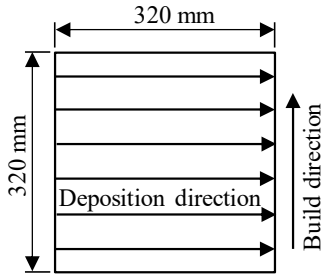


Fig. 4. Typical WAAM coupons extracted in various directions to the print layer direction.

The coupon designation system begins with the WAAM plate type (i.e. A1-A5, as defined in Table 4), followed by the nominal thickness of the plate in mm, the orientation relative to the print layer direction in degrees and a number to identify each individual coupon; a label ending with 'M' denotes a machined coupon, otherwise the coupon was tested in the as-built condition. In total, 137 coupons of different materials, finishes, thicknesses, extraction directions and

135 locations, and deposition strategies, were tested – see Table 4 for details of the test scheme.

136 **Table 4** Summary of WAAM plate types and tested coupons (AB = as-built; M = machined).

Plate type	Deposition strategy	Description	t_{nom} (mm)	Surface	No. of coupons by θ (°)				
					0	30	45	60	90
A1		Reverse deposition direction every layer. Material: Normal-strength steel	8	AB	3	3	3	3	4
				M	3	3	3	3	3
			3	AB	3	3	3	3	4
				M	3	3	3	3	3
A2		Reverse deposition direction every layer. Material: High-strength steel	8	—					
			3	AB	3	3	3	3	5
				M	3	–	3	–	2
A3		Reverse deposition direction every 3 layers. Material: Normal-strength steel	8	AB	4	–	3	–	4
				M	3	–	3	–	3
			3	—					
A4		Half plate printed and fully cooled first; then the second half printed. Reverse deposition direction every layer. Material: Normal-strength steel	8	AB	–	–	–	–	4
				M	–	–	–	–	3
			3	—					
A5		Constant deposition direction. Material: Normal-strength steel	8	AB	3	–	3	–	4
				M	3	–	3	–	3
			3	AB	–	–	–	–	4
				M	—				

3 Geometric measurements

The undulating as-built geometry of the WAAM coupons rendered conventional calliper measurements impractical. Advanced 3D laser scanning, in conjunction with Archimedes' measurements, was therefore employed to determine the geometric properties of both the as-built (AB) and machined (M) coupons. 3D laser scanning was used to capture the specimen geometries, with the scan data verified by Archimedes' principle through comparisons of volume measurements. The volume measurements obtained using laser scanning and Archimedes' principle were consistently within 3%, while the measured densities were also very consistent, with an average value of 7810 kg/m^3 for the normal-strength steel and 7830 kg/m^3 for the high-strength steel. Laser scan data acquisition, processing and geometric characterisation are described in this section.

3.1 Data acquisition and processing

A Faro ScanARM, integrated with a FARO laser line probe, was used to scan all specimens. This laser scanner provides rapid data capture of up to 600000 points per second, with a reported accuracy of 0.1 mm and a resolution of 0.075 mm. Laser scanning of a typical specimen is illustrated in Fig. 5(a). The scan data of each specimen, represented as a point cloud, were converted into a polygon object using the software Geomagic Wrap [31] – see Fig. 5(b). Note that the bottom region of each coupon, which could not be captured by the scanner, was filled by fitting a flat surface to it, to constitute a closed, complete 3D model.

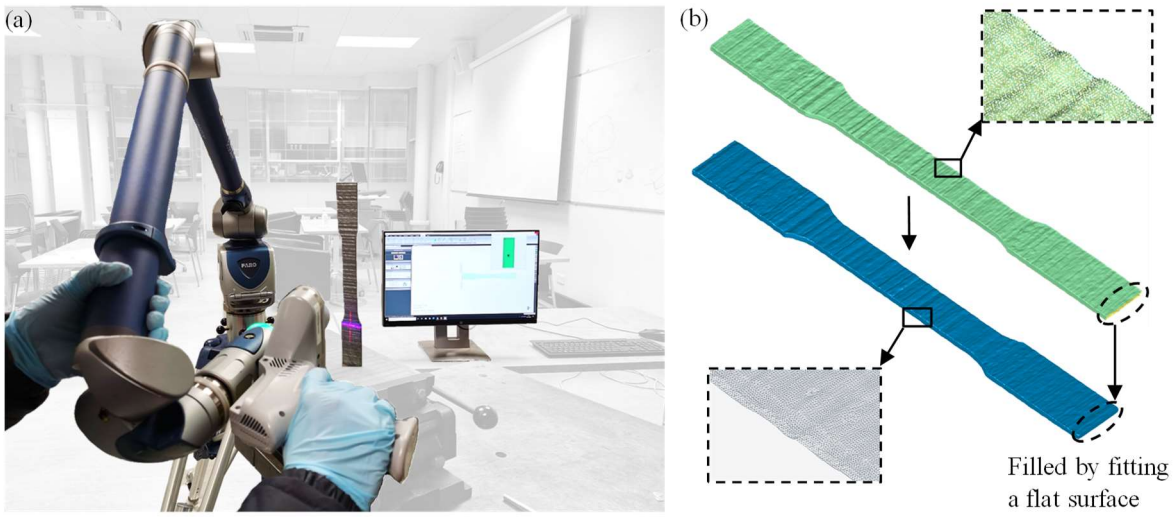


Fig. 5. (a) Laser scanning of a typical coupon; (b) progression of scan data from a point cloud to a polygon object.

The obtained digital model was then saved as a STL file and imported into Rhino 3D [32] for further geometric analysis. The 3D model was reoriented in Rhino using principal component analysis [33,34], such that the overall centroid of the coupon coincided with the origin of the global coordinate system, and the longitudinal axis of the coupon was parallel to the global x axis, as shown in Fig. 6. After alignment, a series of cross-section profiles were extracted from each coupon within the parallel length by means of contouring. For each contour, the cross-sectional area A_i and the deviations of the cross-sectional centroid from the overall centroid of the coupon $e_{y,i}$ and $e_{z,i}$ (along the global y and z axes respectively) were determined. Individual thickness measurements t_i, taken as the distance between the top and bottom surface grid points, were also taken – see Fig. 6.

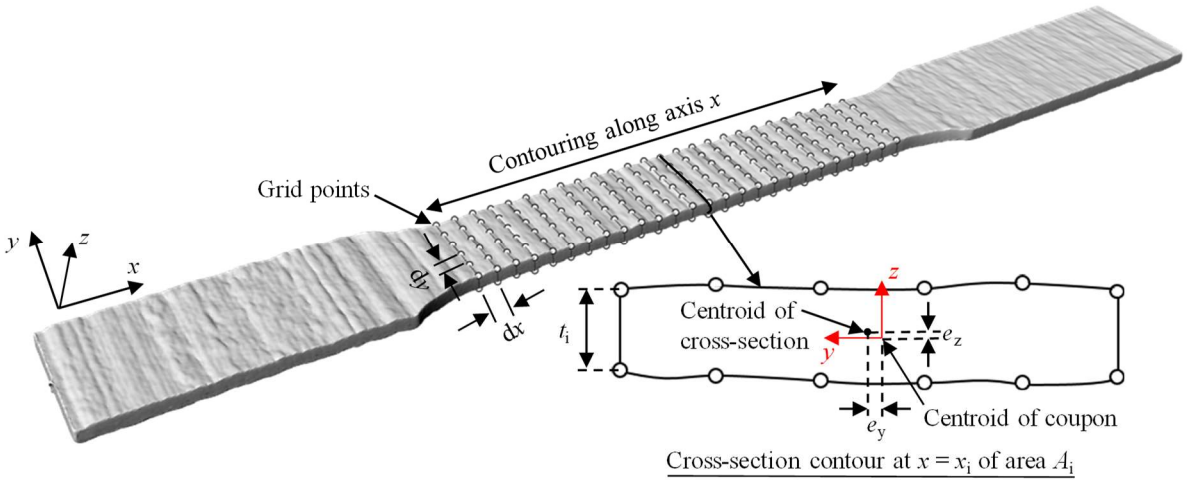


Fig. 6. Typical coupon geometry processed in Rhino 3D [12].

A sensitivity study was performed to determine the most suitable contour spacing that would allow the specimen geometry to be represented with both high computational efficiency and accuracy. Ten as-built coupons (of two nominal thicknesses and five extraction directions) were selected, the geometric measurements of which were taken at contour spacings of 0.05 mm, 0.10 mm, 0.50 mm, 1.00 mm and 2.00 mm; these spacings were all below the typical WAAM layer height, found to vary between about 3 and 5 mm for the thick coupons (t_{nom} = 8 mm), and between about 2 and 3 mm for the thin coupons (t_{nom} = 3 mm). Note that for consistency and simplicity, the contour spacings along x and y axes were kept equal (i.e. dx = dy).

A summary of the results of the sensitivity study is provided in Fig. 7, where the average and minimum cross-sectional area (A and A_{min} respectively) and thickness (t and t_{min} respectively) and the average and maximum centroid eccentricity (e_z and $e_{z,max}$ respectively), as obtained for

the considered contour spacings, are normalised against their corresponding measurements based on dx = 0.05 mm. As expected, the maximum and minimum values of the measurements (i.e. A_{min}, t_{min} and $e_{z,max}$) are shown to be more sensitive to the contour spacing compared to their respective average measurements (i.e. A, t and e_z). It can be observed from Fig. 7 that all normalised measurements generally converge at a contour spacing of 0.10 mm, which was thus adopted in the determination of the specimen geometries.

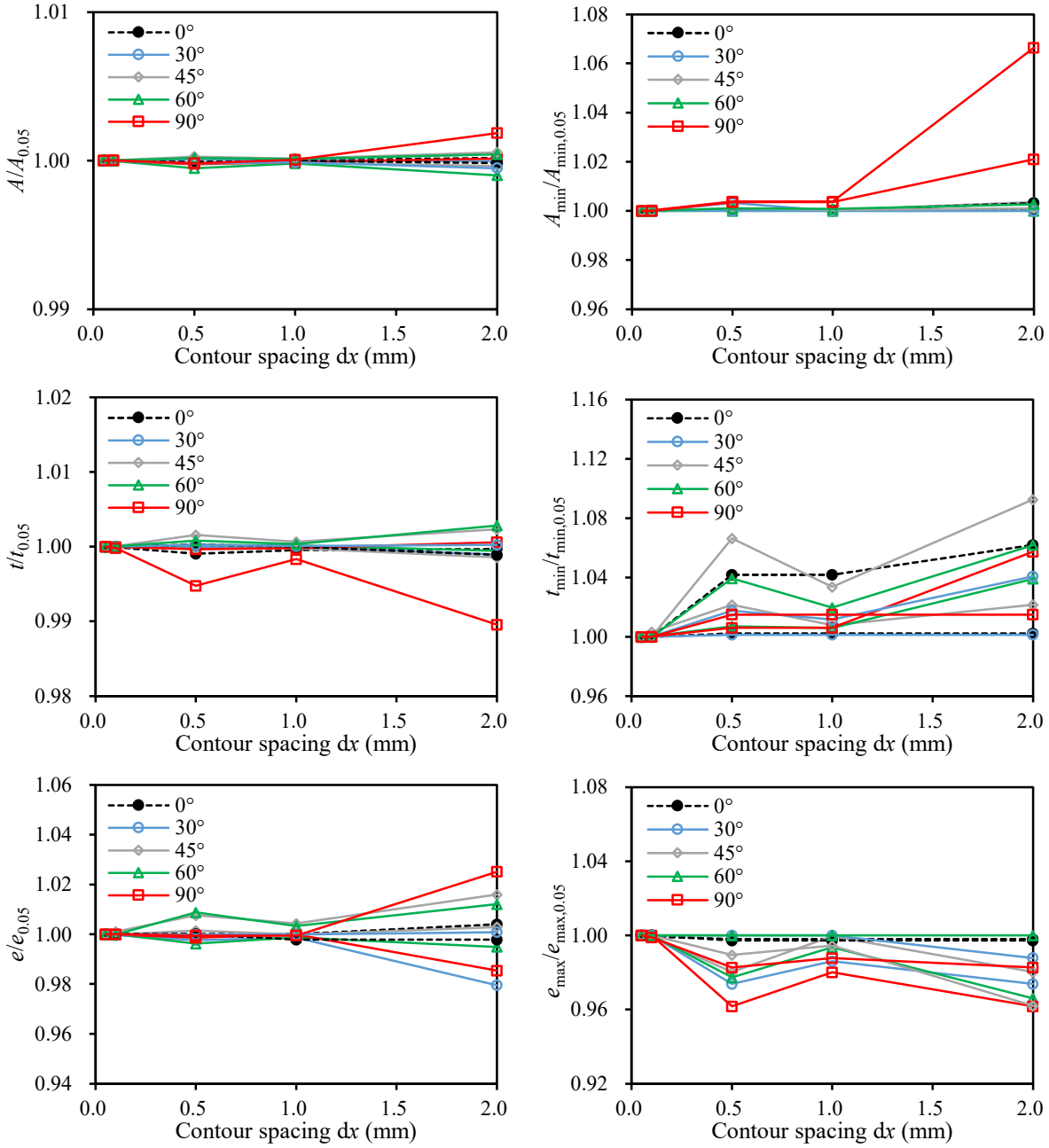


Fig. 7. Results of sensitivity study on contour spacing.

3.2 Geometric properties

The average geometric properties of the as-built coupons are summarised in Table 5, where t_{nom} is the nominal thickness of the coupons, θ denotes the coupon extraction orientation (see Fig. 3(a)), A, A_{min} and A_{sd}, and t, t_{min} and t_{sd}, are the average, minimum and standard deviation values of the cross-sectional area and thickness respectively, e_y is the average centroid eccentricity along the y axis (see Fig. 6), and e_z, $e_{z,max}$ and $e_{z,sd}$ are the average, maximum and standard deviation values of the eccentricity along the z axis respectively.

Table 5 Average geometric properties of as-built coupons.

Plate type	t_{nom} (mm)	θ (°)	A (mm^2)	$\frac{A_{min}}{A}$	$\frac{A_{sd}}{A}$	t (mm)	$\frac{t_{min}}{t}$	$\frac{t_{sd}}{t}$	$\frac{\lvert e_y \rvert}{t}$	$\frac{\lvert e_z \rvert}{t}$	$\frac{\lvert e_z \rvert_{max}}{t}$	$\frac{\lvert e_z \rvert_{sd}}{t}$
A1	8	0	151.4	0.97	0.014	7.48	0.82	0.051	0.011	0.011	0.030	0.008
		30	156.9	0.93	0.035	7.68	0.81	0.065	0.016	0.014	0.041	0.011
		45	151.3	0.92	0.034	7.54	0.82	0.061	0.014	0.024	0.060	0.014
		60	149.0	0.91	0.043	7.43	0.78	0.065	0.015	0.018	0.055	0.013
		90	151.9	0.87	0.049	7.61	0.80	0.064	0.013	0.020	0.073	0.015
	3	0	60.2	0.97	0.012	3.02	0.85	0.038	0.015	0.052	0.067	0.010
		30	59.8	0.96	0.020	2.97	0.85	0.042	0.029	0.064	0.126	0.039
		45	60.0	0.96	0.018	2.97	0.84	0.041	0.028	0.109	0.163	0.037
		60	60.0	0.94	0.023	3.00	0.84	0.043	0.028	0.059	0.122	0.032
		90	59.7	0.90	0.042	3.02	0.83	0.048	0.041	0.171	0.304	0.058
A2	3	0	57.6	0.95	0.021	2.83	0.77	0.055	0.043	0.042	0.069	0.011
		30	57.0	0.93	0.029	2.84	0.73	0.066	0.033	0.085	0.150	0.041
		45	58.0	0.95	0.020	2.87	0.71	0.065	0.024	0.166	0.254	0.058
		60	57.9	0.93	0.027	2.86	0.72	0.076	0.051	0.159	0.349	0.101
		90	56.7	0.92	0.031	2.85	0.71	0.071	0.041	0.276	0.426	0.066
A3	8	0	155.8	0.97	0.014	7.58	0.86	0.044	0.009	0.007	0.019	0.005
		45	162.7	0.93	0.027	7.92	0.83	0.056	0.013	0.040	0.069	0.014
		90	158.4	0.92	0.034	7.81	0.85	0.052	0.015	0.033	0.097	0.023
A4	8	90	151.5	0.90	0.034	7.52	0.83	0.054	0.014	0.023	0.082	0.019
A5	8	0	165.1	0.95	0.015	7.97	0.83	0.051	0.011	0.015	0.034	0.007
		45	157.9	0.96	0.021	7.76	0.86	0.047	0.015	0.007	0.025	0.005
		90	159.5	0.94	0.025	7.86	0.87	0.044	0.014	0.015	0.051	0.011
	3	90	64.6	0.91	0.028	3.20	0.87	0.034	0.024	0.116	0.243	0.060

The as-built plates displayed three main types of surface topography (denoted as profiles A, B and C, as shown in Fig. 8), resulting from different WAAM process parameters. Surface profile A, characterised by discontinuous print layers along the deposition direction, was typically observed in the t_{nom} = 8 mm normal-strength steel plates. Featuring straight and continuous print layers, profile B reflected the surface topography of the t_{nom} = 3 mm normal-strength steel plates, while the less regular surface profile C was mostly seen in the t_{nom} = 3 mm high-strength steel plates. For all plate types, the θ = 0° coupons showed the least variation in thickness t_i and cross-sectional area A_i within the parallel length, while the highest variation in A_i was observed for the θ = 90° coupons. Note that the highest variation in t_i was only exhibited by the θ = 90° coupons with t_{nom} = 3 mm (rather than t_{nom} = 8 mm), attributed to their different surface topographies.

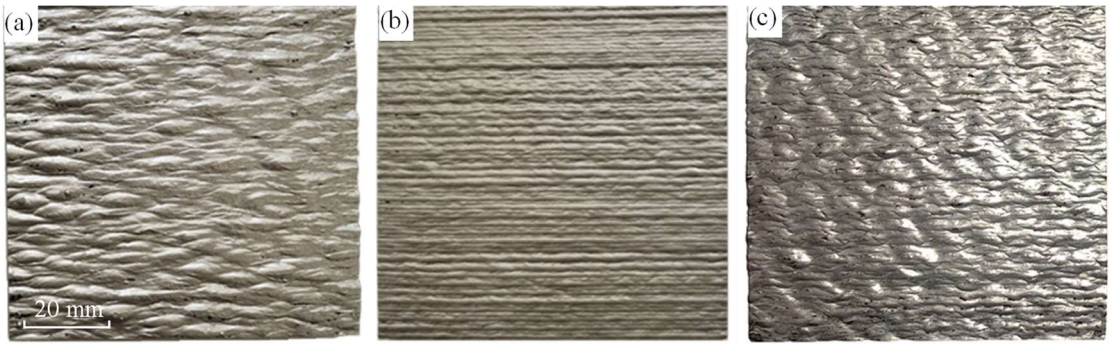


Fig. 8. Surface topography of as-built plates: (a) profile A; (b) profile B; (c) profile C.

Histograms of the measured thicknesses of typical coupons extracted from plates type A1 are presented in Fig. 9, with the individual thickness measurements t_i normalised by the corresponding average coupon thickness t. The histograms show a lower spread of thickness for the t_{nom} = 3 mm coupons compared to the t_{nom} = 8 mm coupons. It can also be observed that apart from the θ = 0° coupons, which exhibit a distinctly narrow spread of thickness, the other coupons display similarly scattered thickness distributions, as reflected by the similar values of t_{sd}/t reported in Table 5. In contrast to the t_{sd}/t values, the values of A_{sd}/A were found, as expected, to be more closely related to the coupon extraction direction. Note that the A_{sd}/A ratio utilised herein is equivalent to the average t_{sd}/t ratio employed in [16] owing to the constant coupon width. The normalised area distributions of typical coupons are presented in Fig. 10, where the spread of area measurements is shown to increase with θ.

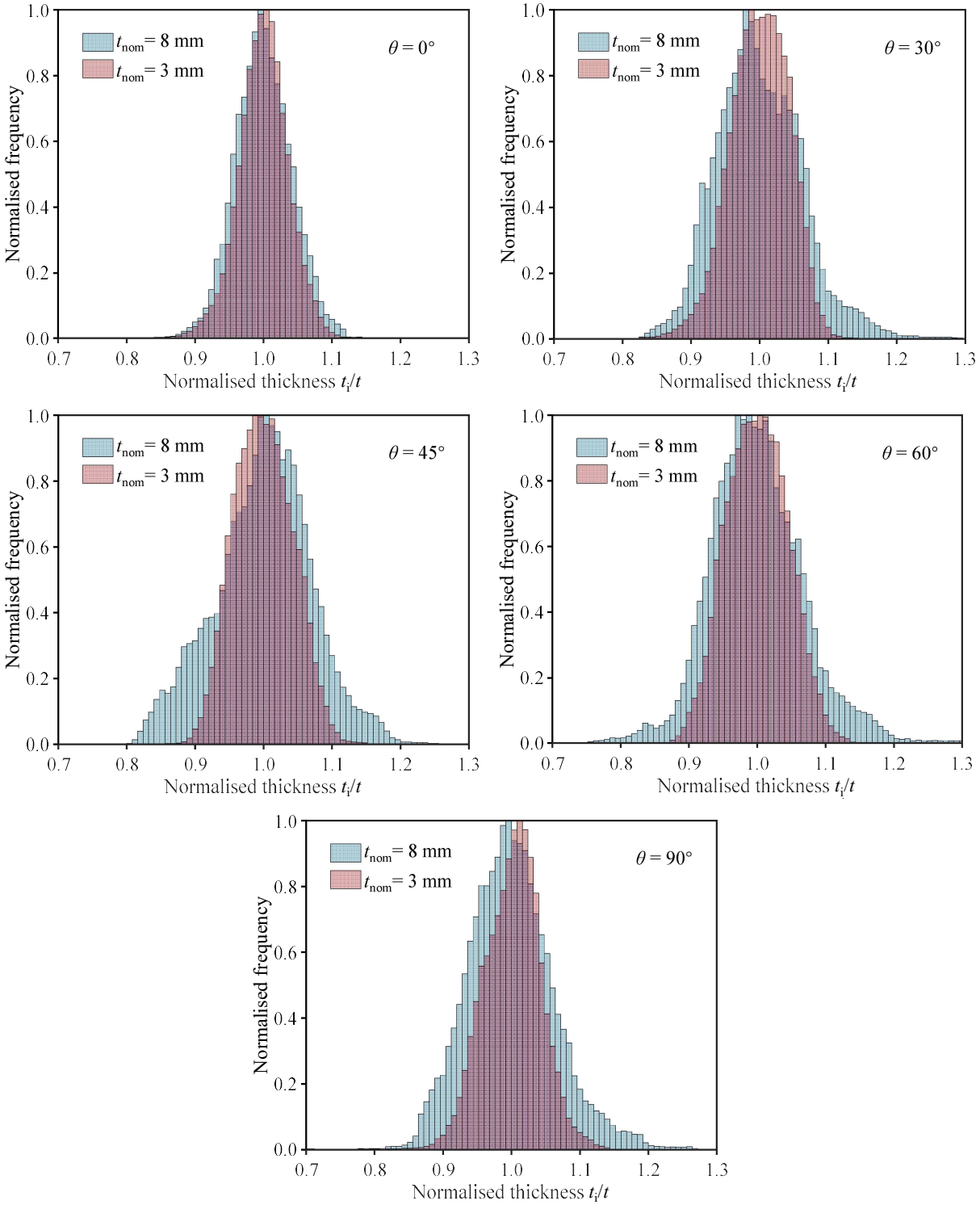


Fig. 9. Distribution of normalised thicknesses t_i/t of as-built coupons extracted from plate type A1.

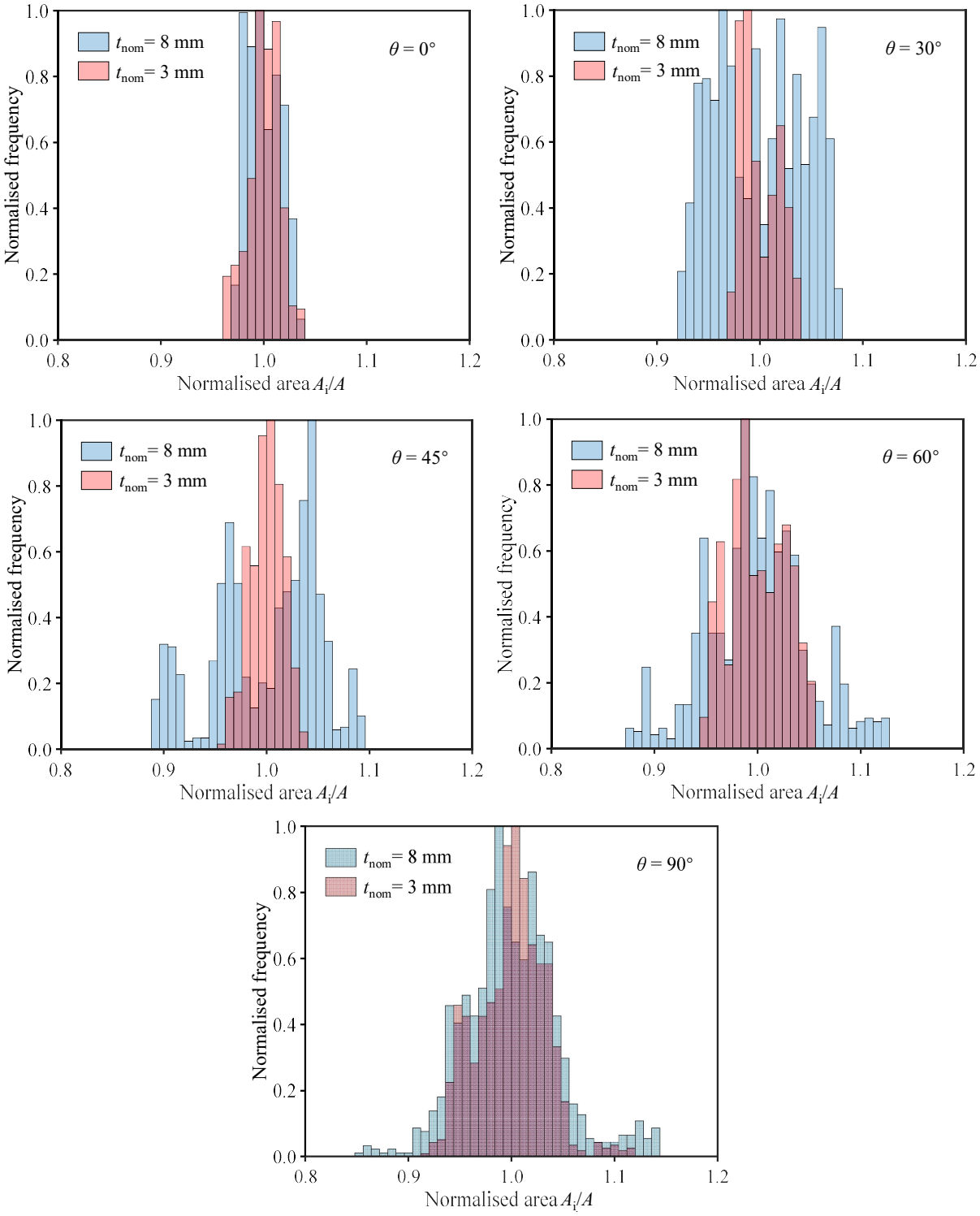


Fig. 10. Distribution of normalised cross-sectional areas A_i/A of as-built coupons extracted from plate type A1.

A comparison of the obtained thickness distributions among coupons of various plate types is presented in Fig. 11. The shapes of the presented histograms reflect the geometric variability associated with the different deposition strategies. The deposition strategy followed for plate type A5 is deemed to provide the least geometric variability among the considered approaches, mirrored by the smallest spread of thicknesses, while, for the same deposition strategy, the

high-strength coupons exhibited greater geometric variation relative to their normal-strength counterparts, as illustrated in both Figs 8 and 11.

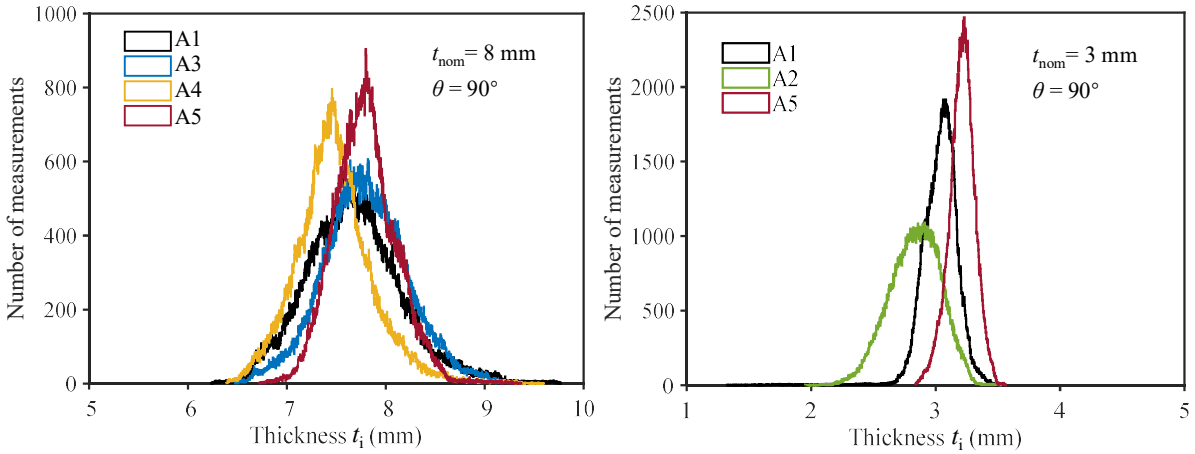
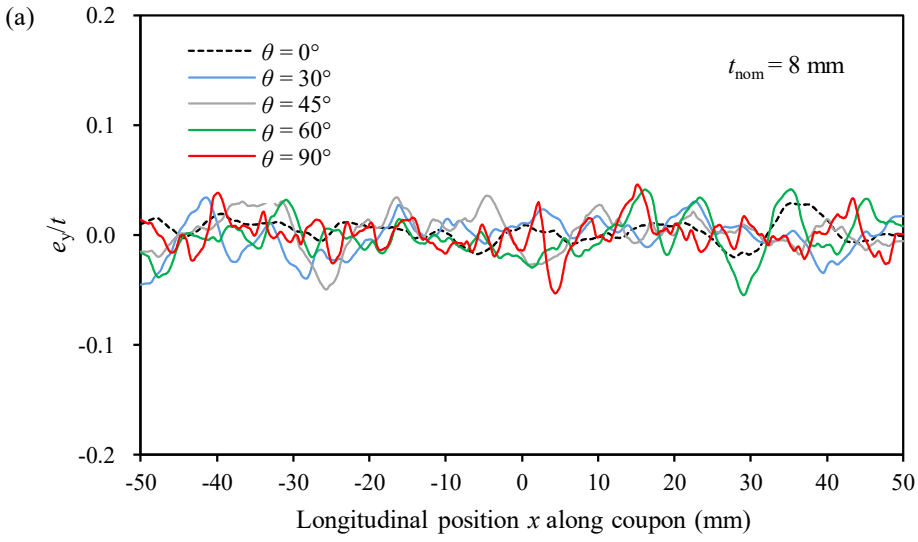
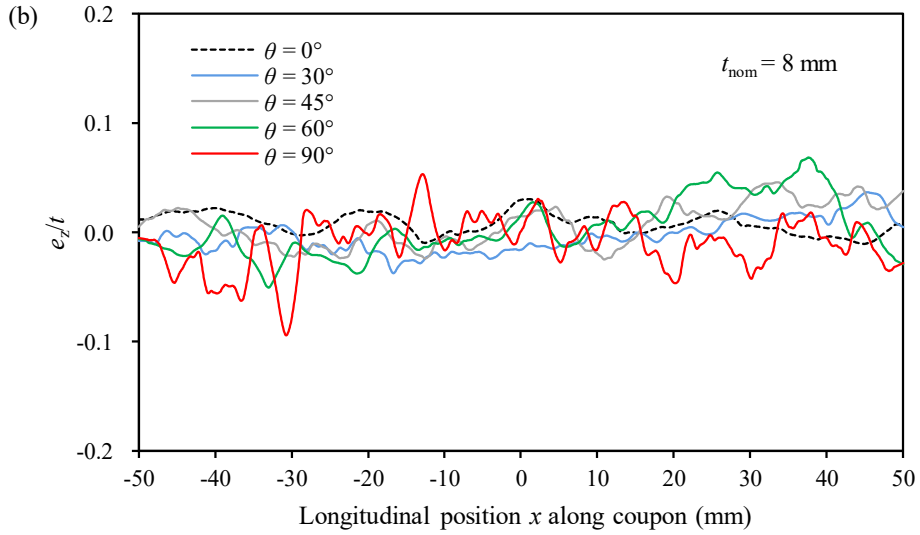


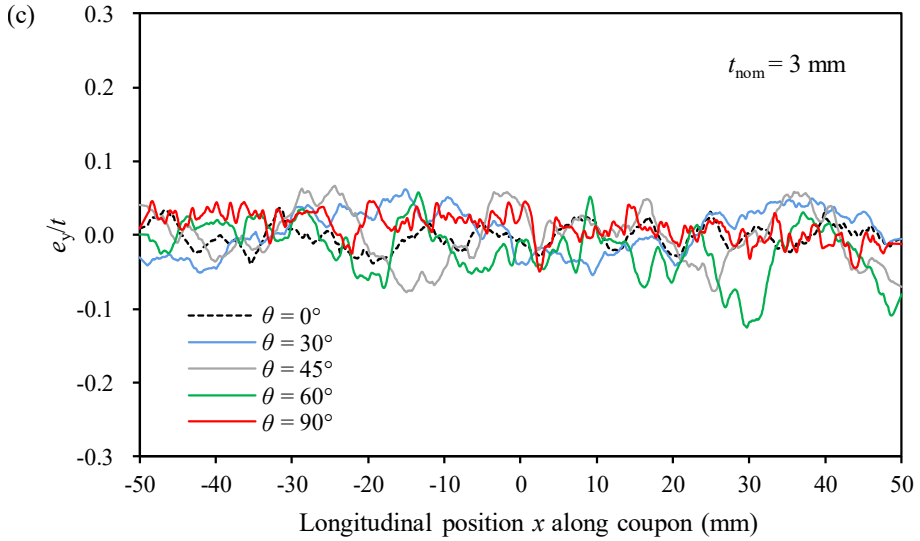
Fig. 11. Comparison of thickness distributions among coupons of various plate types.

Finally, according to Table 5, both the maximum and standard deviation values of the eccentricity along the z axis are shown to be the highest for the $\theta = 90°$ coupons, the lowest for the $\theta = 0°$ coupons, and generally similar for the coupons with $\theta = 30°$, 45° and 60°. This is also confirmed in Fig. 12, where the normalised eccentricities along the y and z axes (e_y/t and e_z/t respectively) are plotted along the coupon length for typical specimens of different nominal thicknesses and directions. Owing to the surface undulations, the eccentricities measured in the z axis direction e_z were generally significantly greater than those in the y axis direction e_y.

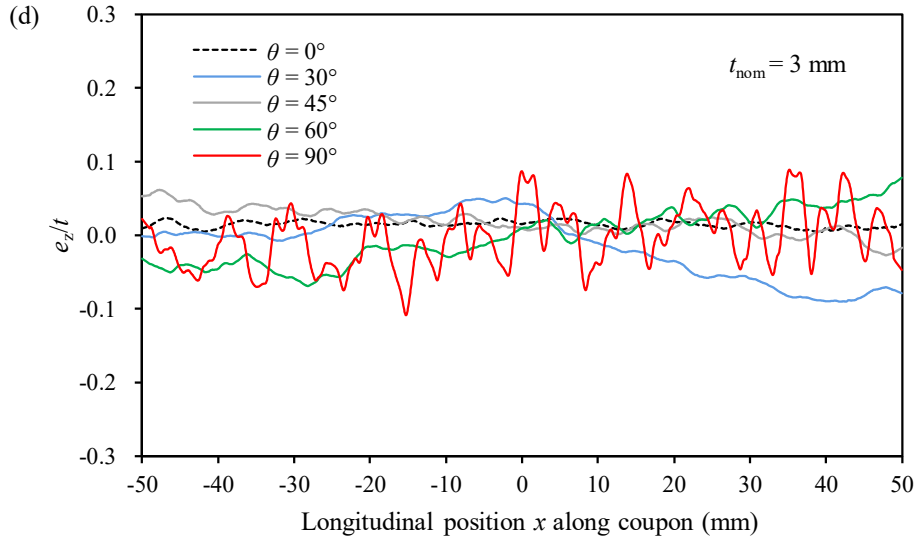




251



252



253

254 **Fig. 12.** Eccentricity measurements along *y* axis and *z* axis of coupons extracted in various directions from plate
255 type A1: (a) and (b) for t_{nom} = 8 mm; (c) and (d) for t_{nom} = 3 mm.

4 Tensile coupon tests

4.1 Test set-up

The stress-strain characteristics of the WAAM materials were determined by means of tensile coupon testing, undertaken at room temperature in accordance with EN ISO 6892-1 [30]. All coupons were tested under uniaxial monotonic loading using a 250 kN Instron 8802 hydraulic testing machine in the Structures Laboratory at Imperial College London.

A four-camera StrainMaster Compact digital image correlation (DIC) LaVision system, with two cameras and an integrated LED illumination source on each side, was employed to monitor the evolution of deformations and strains on both sides of the coupons during testing; the experimental layout adopted for the tensile tests is presented in Fig. 13. The DIC technique provides an accurate and vivid means of describing the full-field deformation behaviour of objects, and its use is of particular importance for as-built WAAM materials, which feature less regular deformation and strain fields compared to conventionally produced materials [35].

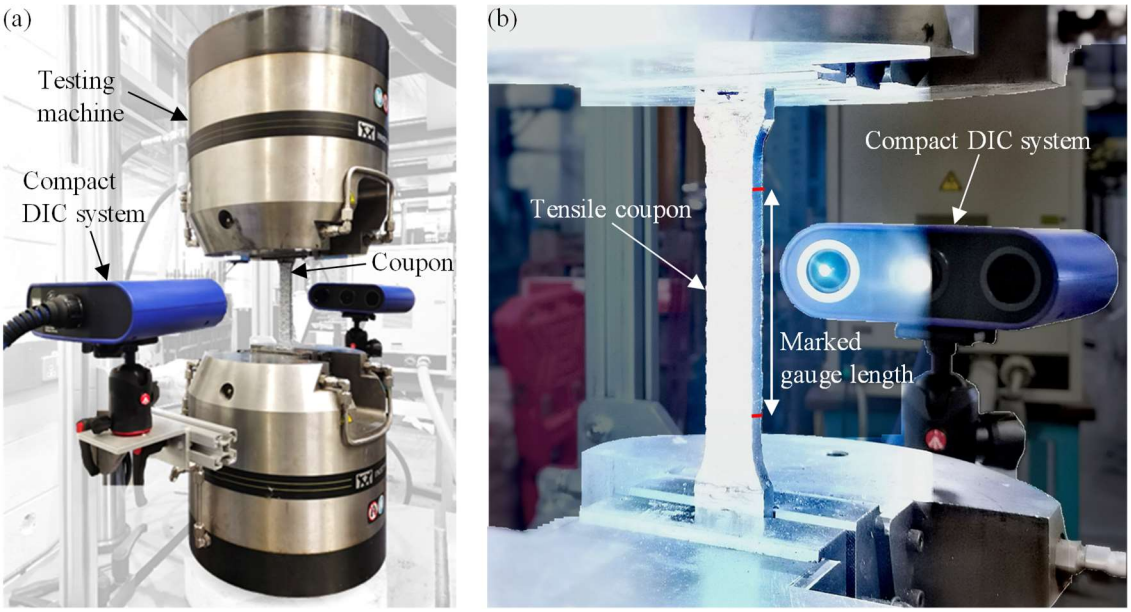


Fig. 13. Tensile test set-up: (a) overview; (b) close-up.

Prior to testing, both the front and back surfaces of the coupons were sprayed with black matt paint within the parallel length, where a random pattern of white speckles was subsequently applied; typical speckled coupons are shown in Fig. 14. The matt paint was adopted to prevent data loss from reflection during image capture, while the black and white high-contrast random speckle pattern facilitated tracking reference points, enabling accurate measurements of deformations. A pair of overlapping standard gauge lengths of $5.65\sqrt{A}$, where A is the average

cross-sectional area of the coupons, as obtained by laser scanning, was marked onto the two side faces of each coupon for the calculation of the fracture strain [30]; a typical marked gauge length is shown in Fig. 13(b).

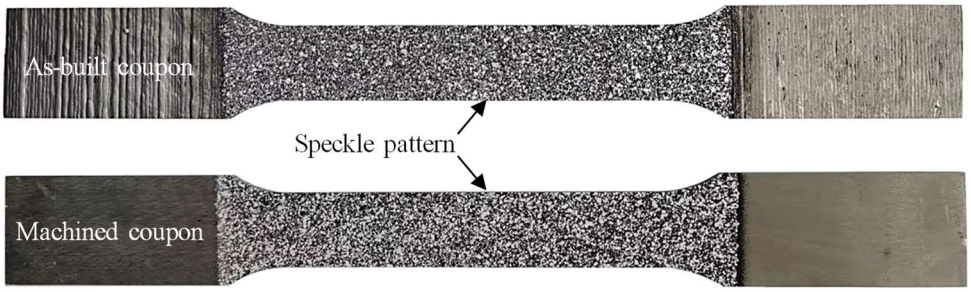


Fig. 14. Typical coupons with a random speckle pattern.

During the tests, the load was applied using displacement control at a strain rate of 0.00007 s^{-1} before yielding, followed by a strain rate of 0.00025 s^{-1} after yielding until failure, with a gradual transition ramp between the two rates. The tensile load was measured by a load cell within the testing machine and the measurements were transmitted to the DIC system through an analogue to digital converter; the received load data, together with the captured DIC images, were then synchronously recorded at a frequency of 1 Hz in the software Davis 10 [36].

Upon completion of the tests, the acquired images were processed in combination with the load data using Davis 10 [36]. The regions over the full parallel length of both sides of each coupon were analysed, within which the relative movements of the surface speckles were determined; the strain distribution was then obtained for each frame. An average stress-strain curve was generated accordingly, with the average stress taken as the applied load divided by the average original cross-sectional area and the average strain determined over the full parallel length of both sides of each coupon.

4.2 Results

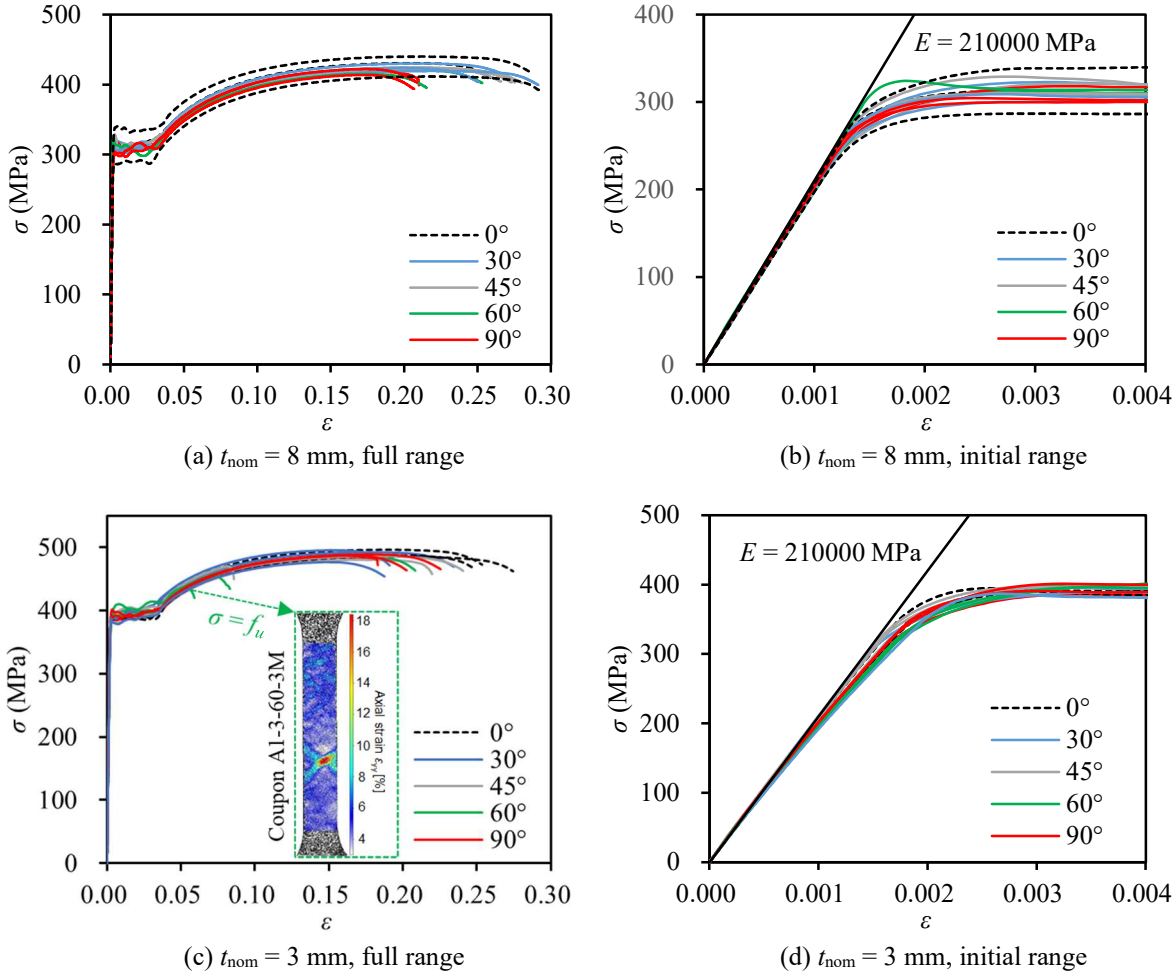
4.2.1 General

The resulting engineering stress-strain curves and material properties of the tested coupons are presented and discussed in this section. In general, the stress-strain characteristics of the WAAM material varied with the feedstock wire and geometric variability of the coupons, with the latter being dependent on the surface finish (i.e. as-built or machined) and extraction direction of the specimens. Key material parameters were derived from the obtained stress-strain curves, including the Young's modulus E, yield strength f_y, ultimate tensile strength f_u,

strain at the ultimate tensile strength ε_u, fracture strain over the marked gauge length ε_f, and Poisson's ratio in the elastic range v. The Young's modulus was determined by regression analysis, as described in [12]. The yield stress was taken as the 0.2% proof stress, since the stress-strain curves were generally slightly rounded, without a sharply-defined yield point. Special attention was paid to the determination of the Poisson's ratio for the WAAM coupons. After filtering the experimental noise associated with the stress-strain curves in both directions (i.e. parallel and perpendicular to the parallel length) using a moving average, the transverse strain ε_x was plotted against the corresponding longitudinal strain ε_y for each coupon. The Poisson's ratio was then calculated using ordinary least squares regression, and was taken as the average slope of the ε_x versus ε_y curve in the elastic range between $0.1f_y$ and $0.3f_y$; further details can be found in [37].

4.2.2 Machined coupons

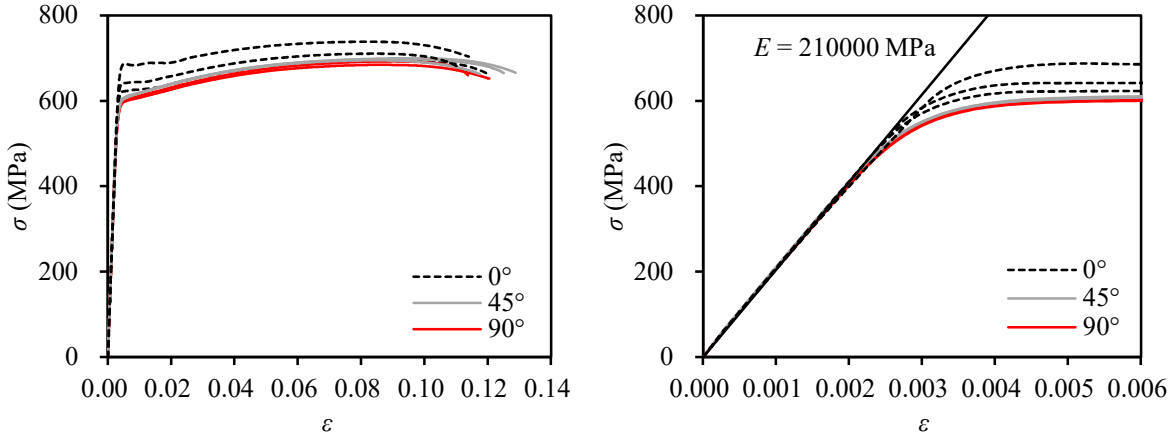
The initial and full ranges of the engineering stress-strain curves of the machined coupons extracted from plate types A1-A5 are presented in Figs 15-19, respectively. A summary of the average material properties, grouped by plate type (i.e. A1-A5), nominal thickness t_{nom} and coupon extraction direction θ, is provided in Table 6, while the material properties of the nominally 8 mm and 3 mm thick machined coupons are reported in Tables 7 and 8, respectively. It can be observed from Figs 15-19 that the machined normal-strength coupons exhibited a stress-strain response similar to that of hot-rolled steels, characterised by a well-defined yield point, a yield plateau and subsequent strain hardening [38]. However, most of the high-strength coupons displayed a somewhat rounded stress-strain response, with no distinct yield point or yield plateau – see Fig. 16. Although strain hardening was observed for both the normal- and high-strength steels, it was much less pronounced for the latter, as apparent from Figs 15-19. This is also reflected by the values of f_u/f_y in Tables 6-8, where the $t_{nom} = 3$ mm machined high-strength steel coupons exhibit lower values of f_u/f_y than the corresponding normal-strength steel coupons (1.14 versus 1.23 on average), indicating less significant strain hardening.



(a) t_{nom} = 8 mm, full range (b) t_{nom} = 8 mm, initial range

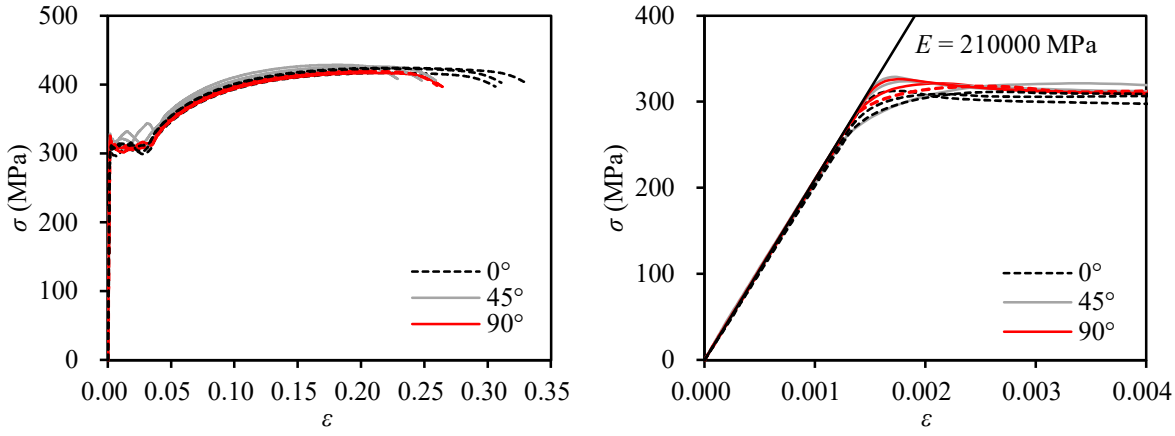
(c) t_{nom} = 3 mm, full range (d) t_{nom} = 3 mm, initial range

Fig. 15. Stress-strain curves of machined coupons from plate type A1.



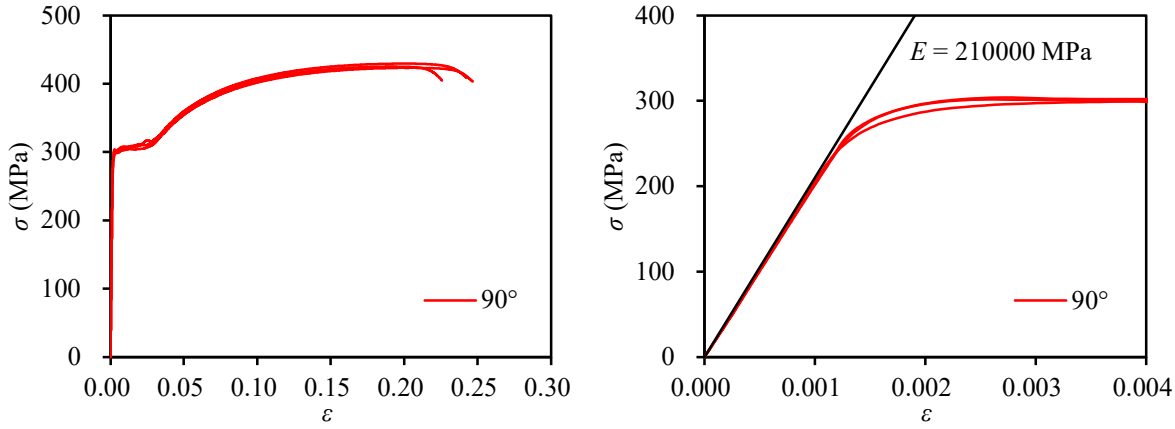
(a) t_{nom} = 3 mm, full range (b) t_{nom} = 3 mm, initial range

Fig. 16. Stress-strain curves of machined coupons from plate type A2 (high-strength steel).



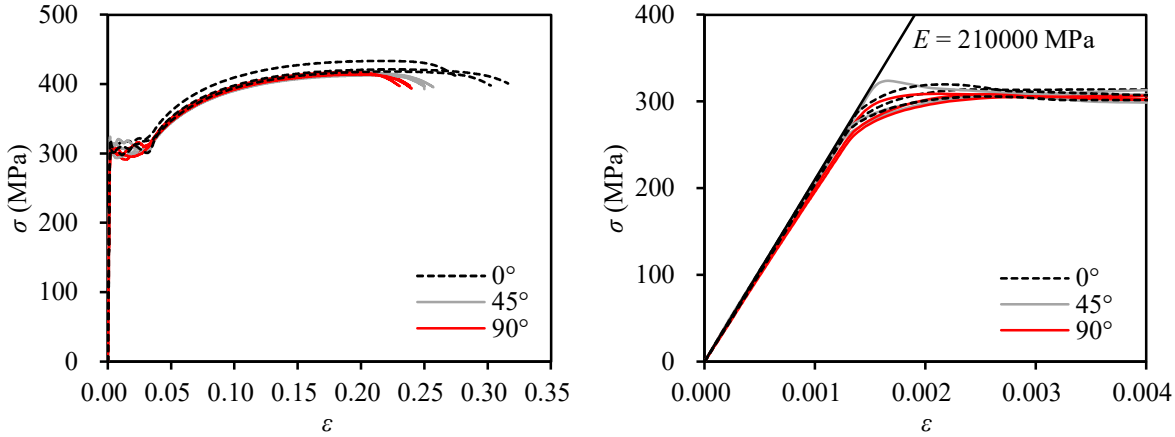
(a) t_{nom} = 8 mm, full range (b) t_{nom} = 8 mm, initial range

Fig. 17. Stress-strain curves of machined coupons from plate type A3.



(a) t_{nom} = 8 mm, full range (b) t_{nom} = 8 mm, initial range

Fig. 18. Stress-strain curves of machined coupons from plate type A4.



(a) t_{nom} = 8 mm, full range (b) t_{nom} = 8 mm, initial range

Fig. 19. Stress-strain curves of machined coupons from plate type A5.

348 **Table 6** Average material properties of machined coupons.

Plate type	t_{nom} (mm)	θ (°)	E (MPa)	v	f_y (MPa)	f_u (MPa)	ε_u	ε_f	f_u/f_y	$\varepsilon_u/\varepsilon_y$
A1	8	0	201200	0.28	312	428	0.21	0.38	1.38	60.0
		30	200500	0.30	310	424	0.21	0.38	1.37	58.7
		45	199700	0.25	319	424	0.21	0.37	1.33	57.3
		60	204500	0.27	311	420	0.20	0.35	1.35	55.4
		90	204500	0.29	307	418	0.17	0.31	1.36	49.6
	3	0	211500	0.26	390	490	0.19	0.38	1.26	49.0
		30	212400	0.28	387	483	0.16	0.35	1.25	41.7
		45	222200	0.28	392	479	0.14	0.32	1.22	37.8
		60	212500	0.25	397	459	0.10	0.21	1.16	24.9
		90	215700	0.29	392	486	0.17	0.33	1.24	44.1
A2	3	0	220400	0.28	651	715	0.08	0.22	1.10	17.2
		45	224900	0.28	604	698	0.09	0.23	1.16	19.6
		90	221600	0.28	598	689	0.09	0.21	1.15	18.6
A3	8	0	205600	0.26	305	421	0.23	0.44	1.38	65.1
		45	216300	0.28	315	427	0.19	0.35	1.36	56.2
		90	212000	0.30	311	419	0.21	0.38	1.35	60.8
A4	8	90	197800	0.29	300	426	0.20	0.33	1.42	56.2
A5	8	0	206400	0.28	308	424	0.22	0.42	1.38	63.0
		45	208800	0.28	307	415	0.20	0.38	1.35	58.2
		90	204500	0.26	305	416	0.19	0.34	1.37	55.0

349

350

351 **Table 7** Material properties of machined coupons of 8 mm nominal thickness.

Coupon	E (MPa)	v	f_y (MPa)	f_u (MPa)	ε_u	ε_f	f_u/f_y	$\varepsilon_u/\varepsilon_y$
A1-8-0-1M	202700	0.29	309	431	0.20	0.36	1.39	57.3
A1-8-0-2M	193200	0.28	287	412	0.22	0.39	1.44	64.1
A1-8-0-3M	207700	0.28	339	440	0.21	0.40	1.30	58.6
A1-8-30-1M	201300	0.30	322	430	0.21	0.38	1.34	58.1
A1-8-30-2M	204700	0.29	306	424	0.20	0.35	1.38	56.4
A1-8-30-3M	195500	0.29	302	420	0.22	0.40	1.39	61.5
A1-8-45-1M	197300	0.23	310	424	0.20	0.39	1.37	57.1
A1-8-45-2M	208600	0.27	325	425	0.20	0.37	1.31	56.4
A1-8-45-3M	193100	0.26	321	424	0.21	0.37	1.32	58.4
A1-8-60-1M	195800	0.28	311	422	0.20	0.36	1.36	56.3
A1-8-60-2M	198200	0.27	309	422	0.21	0.39	1.37	59.3
A1-8-60-3M	219700	0.27	314	415	0.17	0.31	1.32	50.5
A1-8-90-1M	201200	0.30	318	419	0.18	0.34	1.32	49.4
A1-8-90-2M	203700	0.27	303	414	0.17	0.29	1.37	48.8
A1-8-90-3M	208700	0.30	300	422	0.17	0.31	1.41	50.6
A3-8-0-1M	213000	0.27	299	417	0.22	0.45	1.39	66.0
A3-8-0-2M	204000	0.24	306	424	0.23	0.44	1.39	66.1
A3-8-0-3M	199700	0.27	310	423	0.22	0.42	1.37	63.3
A3-8-45-1M	227500	0.29	311	429	0.18	0.34	1.38	53.7
A3-8-45-2M	204800	0.27	321	426	0.20	0.36	1.33	56.6
A3-8-45-3M	216500	0.28	313	426	0.20	0.36	1.36	58.3
A3-8-90-1M	215700	0.30	311	417	0.21	0.38	1.34	61.5
A3-8-90-2M	208300	0.31	311	419	0.21	0.36	1.35	60.5
A3-8-90-3M	211900	0.30	311	420	0.21	0.39	1.35	60.4
A4-8-90-1M	197400	0.28	302	430	0.19	0.34	1.42	55.1
A4-8-90-2M	198400	0.30	300	423	0.21	0.33	1.41	59.0
A4-8-90-3M	197600	0.30	299	425	0.19	0.32	1.42	54.4
A5-8-0-1M	204800	0.26	314	433	0.22	0.39	1.38	61.4
A5-8-0-2M	213100	0.29	309	421	0.22	0.44	1.36	64.5
A5-8-0-3M	201400	0.28	302	418	0.22	0.44	1.39	63.0
A5-8-45-1M	200400	0.30	312	416	0.20	0.38	1.33	57.3
A5-8-45-2M	218200	0.28	308	417	0.20	0.37	1.35	57.3
A5-8-45-3M	207800	0.27	300	413	0.21	0.39	1.37	60.0
A5-8-90-1M	212700	0.26	303	417	0.19	0.35	1.38	54.9
A5-8-90-2M	197100	0.25	306	414	0.20	0.34	1.35	55.8
A5-8-90-3M	203700	0.27	305	417	0.19	0.33	1.37	54.4

352 **Table 8** Material properties of machined coupons of 3 mm nominal thickness.

Coupon	E (MPa)	v	f_y (MPa)	f_u (MPa)	ε_u	ε_f	f_u/f_y	$\varepsilon_u/\varepsilon_y$
A1-3-0-1M	209600	0.26	393	496	0.19	0.37	1.26	48.8
A1-3-0-2M	206900	0.25	386	488	0.18	0.34	1.26	46.9
A1-3-0-3M	217900	0.27	390	485	0.19	0.43	1.24	51.3
A1-3-30-1M	220900	0.29	387	479	0.15	0.34	1.24	40.7
A1-3-30-2M	208300	0.31	394	492	0.18	0.34	1.25	45.9
A1-3-30-3M	208000	0.25	381	476	0.15	0.38	1.25	38.7
A1-3-45-1M	220200	0.29	383	480	0.17	0.36	1.25	44.2
A1-3-45-2M	216200	0.29	396	486	0.18	0.41	1.23	47.2
A1-3-45-3M	230400	0.28	396	470	0.08	0.19	1.19	22.0
A1-3-60-1M	202500	0.24	397	487	0.16	0.31	1.23	41.4
A1-3-60-2M	217300	0.25	396	454	0.08	0.20	1.15	19.6
A1-3-60-3M	217600	0.26	400	437	0.05	0.12	1.09	13.8
A1-3-90-1M	222000	0.29	385	484	0.17	0.34	1.26	45.0
A1-3-90-2M	212500	0.28	389	487	0.16	0.32	1.25	42.6
A1-3-90-3M	212700	0.31	400	489	0.17	0.35	1.22	44.7
A2-3-0-1M	224200	0.27	622	697	0.09	0.22	1.12	18.6
A2-3-0-2M	222100	0.26	642	711	0.08	0.21	1.11	17.3
A2-3-0-3M	214700	0.29	688	739	0.08	0.24	1.07	15.7
A2-3-45-1M	222000	0.25	606	700	0.10	0.27	1.16	20.5
A2-3-45-2M	226100	0.30	602	695	0.09	0.23	1.15	18.4
A2-3-45-3M	226900	0.29	603	698	0.09	0.21	1.16	19.8
A2-3-90-1M	222400	0.28	600	693	0.09	0.23	1.15	19.2
A2-3-90-2M	220900	0.29	596	685	0.08	0.18	1.15	18.1

353

354 The WAAM process resulted in the deposited material having lower strength compared to the
355 values stated by the manufacturer for conventional welds, with the observed differences being
356 more pronounced for the normal-strength steel than for the high-strength steel, and for the
357 thicker coupons (t_{nom} = 8 mm). This reflects the slower cooling rates and longer $t_{8/5}$ times
358 associated with the WAAM process, as discussed further in Section 4.3. The measured Young's
359 moduli (mostly between 195 and 225 GPa) and Poisson's ratios (mostly between 0.27 and
360 0.30), on the other hand, generally fell within the range typically seen for conventional steels
361 [39,40].

362 The tested coupons generally exhibited good ductility, with almost all satisfying the Eurocode
363 3 ductility requirements for hot-rolled steels, i.e. $f_u/f_y \geq 1.10$ and $\varepsilon_f \geq 15\%$ for normal-strength
364 steels, as specified in EN 1993-1-1 [39], and $f_u/f_y \geq 1.05$, $\varepsilon_f \geq 10\%$ and $\varepsilon_u/\varepsilon_y \geq 15$ for high-

strength steels, as specified in EN 1993-1-12 [41]. Exceptions to this were two normal-strength steel coupons — A1-3-60-2M and A1-3-60-3M, where premature fracture occurred, possibly due to a lack of fusion. The axial strain distribution in Coupon A1-3-60-3M, as obtained from the DIC results at the point where the average applied stress is equal to f_y, is shown in Fig. 15 (c); the high localised strain concentration indicates the location of the premature fracture.

Fig. 20 shows typical fractured machined coupons of various extraction directions, along with the axial strain distributions visualised by DIC at the point of fracture. It can be observed that the machined coupons all displayed fairly consistent patterns of necking, despite their different extraction directions.

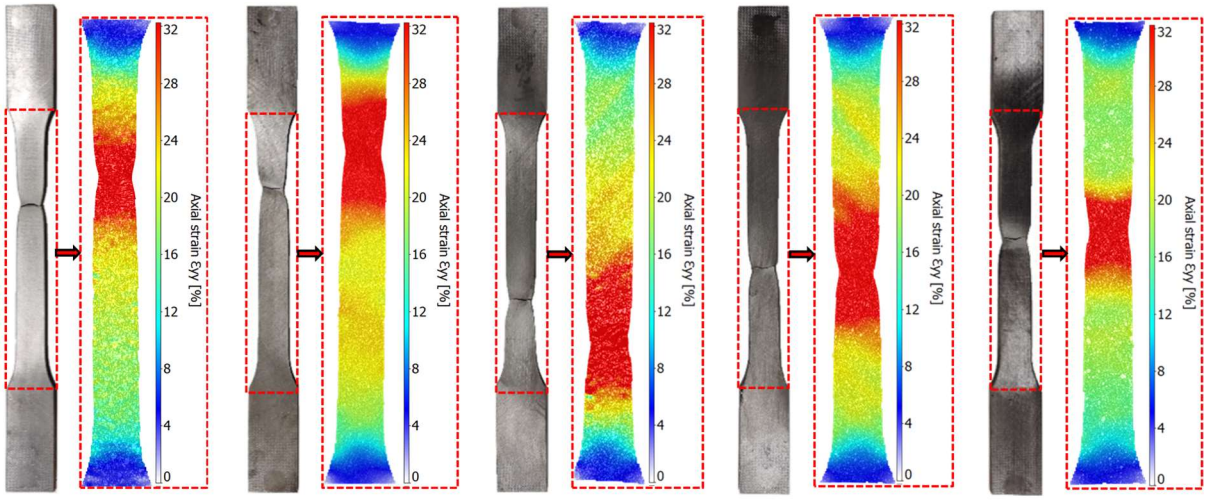


Fig. 20. Typical t_{nom} = 8 mm machined normal-strength steel coupons after fracture, with DIC axial strain plots at fracture.

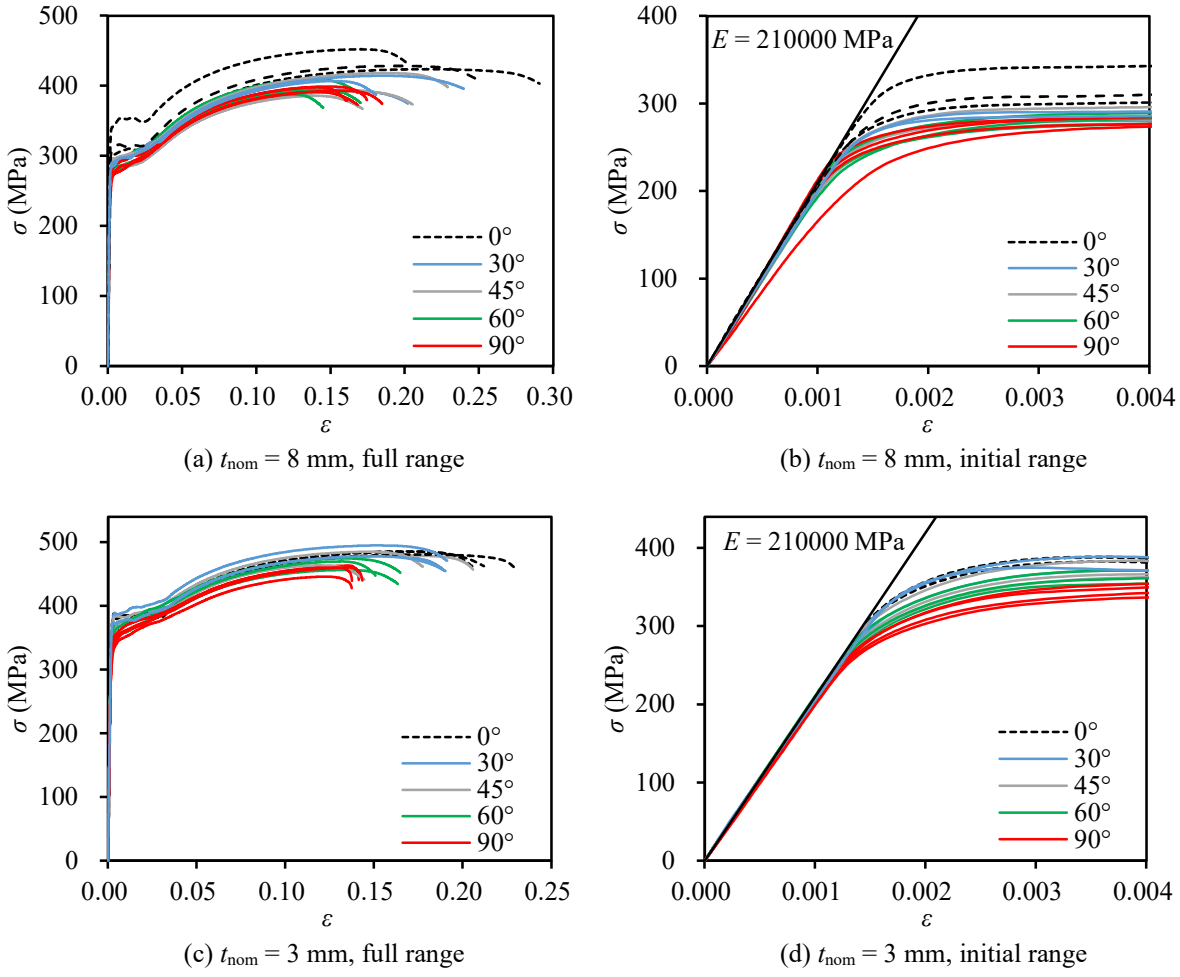
4.2.3 As-built coupons

The full engineering stress-strain curves, alongside their initial segments, of the as-built coupons extracted from plate types A1-A5 are plotted in Figs 21-25, respectively. A summary of the average effective material properties is given in Table 9, and the effective material properties of the individual t_{nom} = 8 mm and 3 mm as-built coupons are reported in Tables 10 and 11, respectively. Note that, owing to the geometric variability, the material properties of the as-built coupons were calculated based on their average cross-sectional area determined by laser scanning and are termed ‘effective’.

As can be seen from Figs 21-25, the overall form of the stress-strain curves of the as-built coupons generally match that of the machined coupons. However, some differences can be

observed, as described below. Apart from some $\theta = 0°$ coupons, the vast majority of the as-built normal-strength coupons featured a slightly inclined (rather than flat) yield plateau, arising from the undulating as-built geometry. The stress-strain response of the as-built high-strength coupons was also shown to be slightly more rounded compared to their machined counterparts.

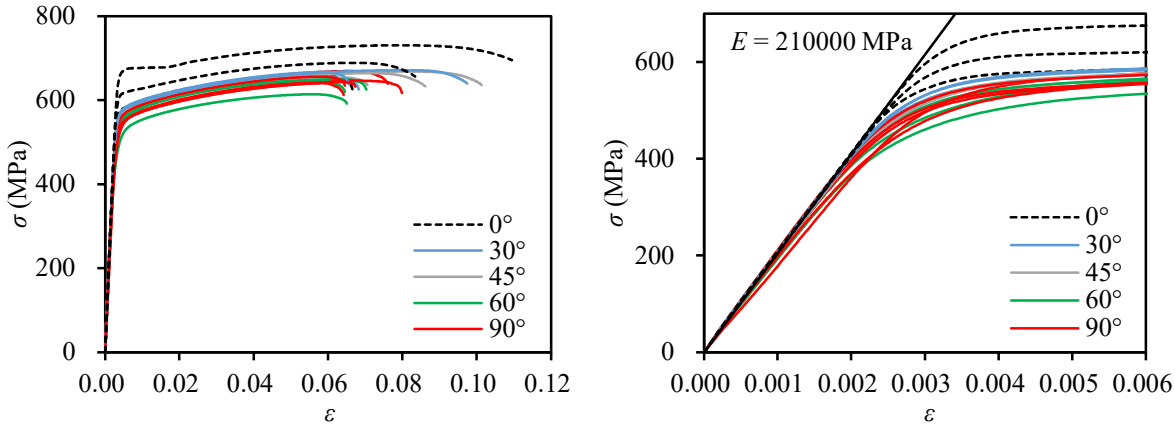
Similar to the machined coupons, the as-built coupons exhibited comparable Young's modulus values to that of conventional steels, but lower strength relative to the manufacturer's measured values on as-welded material. Regarding the ductility of the as-built coupons, despite being inferior to that of their equivalent machined coupons, the Eurocode 3 ductility requirements for hot-rolled steels, as listed in the previous subsection, were nonetheless satisfied.



(a) t_{nom} = 8 mm, full range (b) t_{nom} = 8 mm, initial range

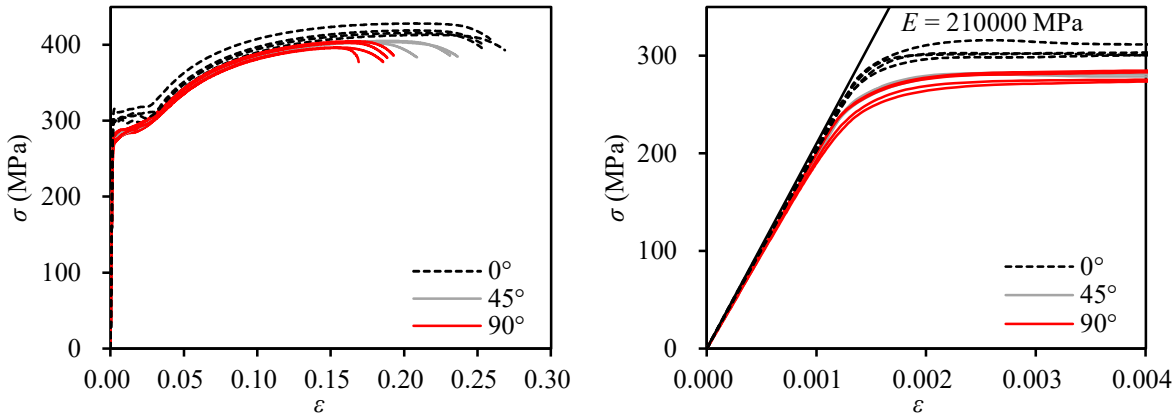
(c) t_{nom} = 3 mm, full range (d) t_{nom} = 3 mm, initial range

Fig. 21. Stress-strain curves of as-built coupons from plate type A1.



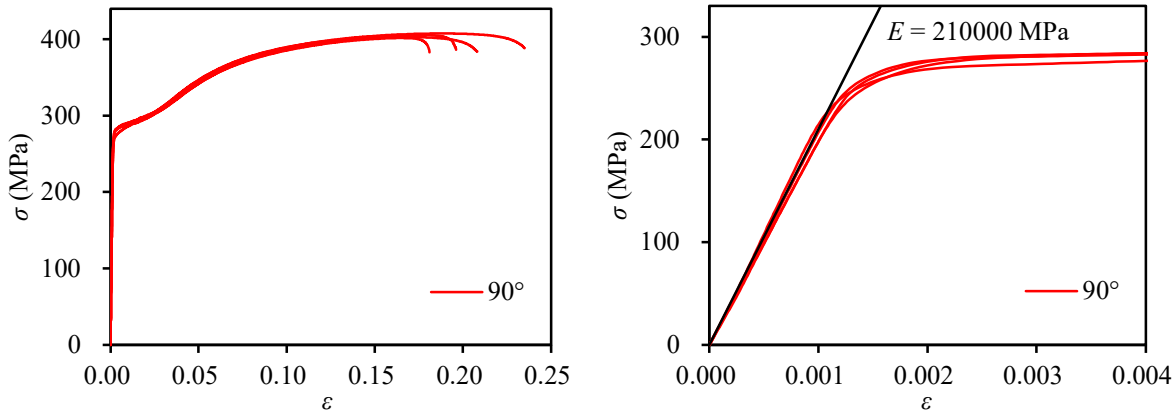
(a) t_{nom} = 3 mm, full range (b) t_{nom} = 3 mm, initial range

Fig. 22. Stress-strain curves of as-built coupons from plate type A2 (high-strength steel).



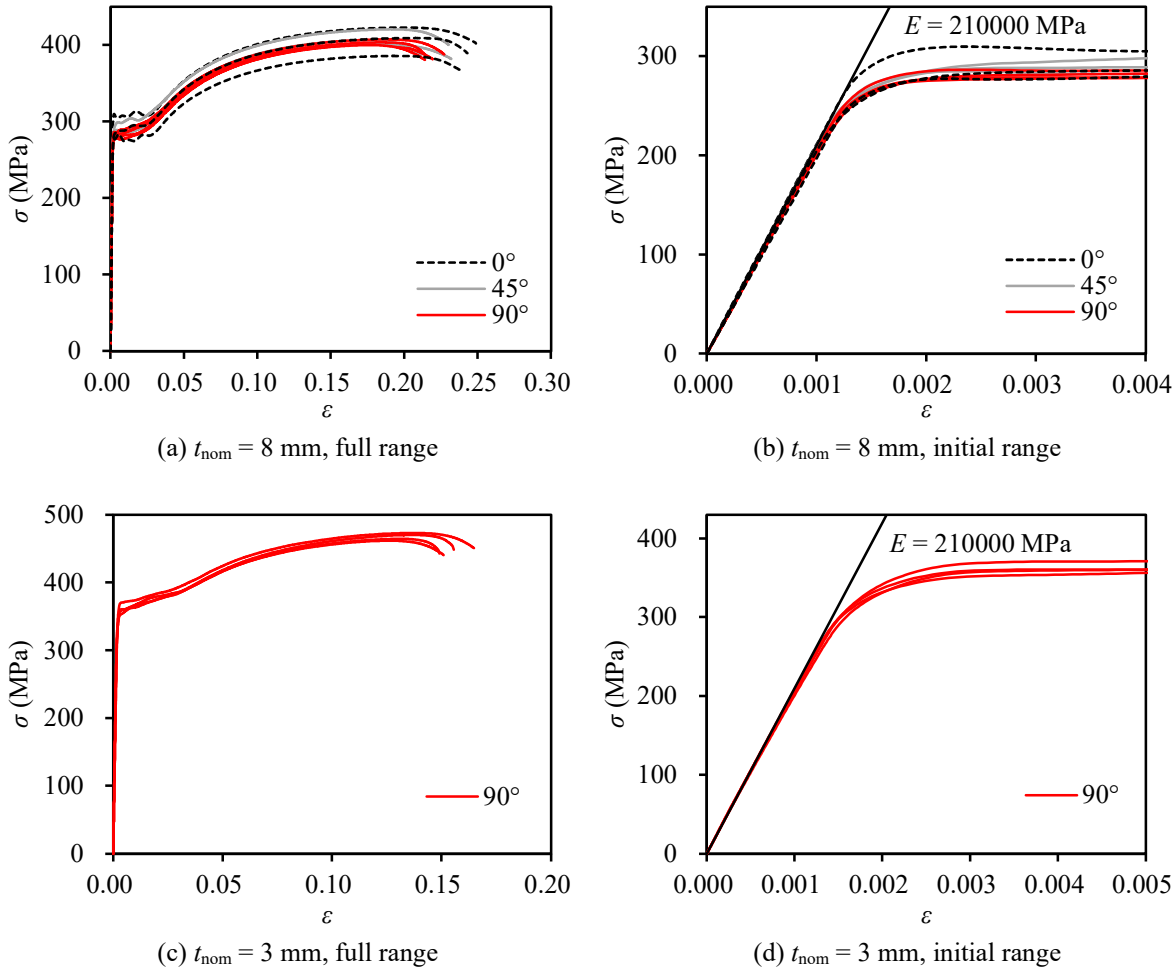
(a) t_{nom} = 8 mm, full range (b) t_{nom} = 8 mm, initial range

Fig. 23. Stress-strain curves of as-built coupons from plate type A3.



(a) t_{nom} = 8 mm, full range (b) t_{nom} = 8 mm, initial range

Fig. 24. Stress-strain curves of as-built coupons from plate type A4.



(a) t_{nom} = 8 mm, full range (b) t_{nom} = 8 mm, initial range

(c) t_{nom} = 3 mm, full range (d) t_{nom} = 3 mm, initial range

Fig. 25. Stress-strain curves of as-built coupons from plate type A5.

Typical fractured as-built normal-strength steel coupons of the two nominal thicknesses (i.e. t_{nom} = 8 mm and 3 mm), alongside the corresponding axial strain distributions at fracture derived from DIC, are shown in Figs 26 and 27, respectively, while typical high-strength steel coupons (t_{nom} = 3 mm) after fracture, together with the DIC axial strain plots, are presented in Fig. 28. As shown from the DIC plots, the as-built coupons exhibited less uniformly distributed strain fields than those displayed by the machined coupons due to the undulating geometry. Furthermore, the strain distributions reflect, to some extent, the coupon extraction directions; this observation is more pronounced for the normal-strength steel coupons than for the high-strength steel coupons, due to the different surface topographies – see Fig. 8. Note the more severe concentration of strains at fracture for the θ = 90° coupon in comparison to the other coupon extraction directions; this is shown in Fig. 27 and caused by the existence of troughs in the printed geometry and hence regions of lower cross-sectional area where deformations accumulate. This results in reduced fracture strains when measured over the standard gauge

length. Finally, it is worth mentioning that, as expected, the as-built coupons generally fractured at their minimum cross-section (as identified from the laser scan data), i.e. the cross-section of minimum average thickness, as illustrated in Fig. 29.

Table 9 Average effective material properties of as-built coupons.

Plate type	t_{nom} (mm)	θ (°)	E (MPa)	v	f_y (MPa)	f_u (MPa)	ε_u	ε_f	f_u/f_y	$\varepsilon_u/\varepsilon_y$
A1	8	0	206700	0.28	317	435	0.19	0.34	1.37	54.8
		30	199700	0.29	285	405	0.17	0.31	1.42	48.3
		45	194100	0.27	285	399	0.17	0.29	1.40	47.7
		60	196700	0.29	281	397	0.14	0.24	1.41	39.6
		90	188400	0.28	278	395	0.15	0.23	1.42	42.1
	3	0	213700	0.28	386	484	0.17	0.34	1.25	45.5
		30	215100	0.25	378	484	0.15	0.37	1.28	40.3
		45	208500	0.27	371	476	0.15	0.28	1.29	38.4
		60	209300	0.28	362	467	0.13	0.28	1.29	35.8
		90	201200	0.29	345	458	0.13	0.20	1.33	35.0
A2	3	0	218300	0.27	623	693	0.07	0.16	1.11	14.0
		30	218800	0.28	571	665	0.07	0.18	1.16	14.2
		45	217400	0.28	560	662	0.07	0.15	1.18	15.7
		60	212200	0.27	536	637	0.06	0.13	1.19	12.9
		90	211800	0.28	550	651	0.06	0.12	1.18	13.5
A3	8	0	206700	0.28	304	419	0.21	0.34	1.38	60.7
		45	195200	0.26	281	404	0.18	0.32	1.44	53.1
		90	193500	0.25	278	400	0.16	0.23	1.44	46.1
A4	8	90	199100	0.28	281	405	0.17	0.28	1.44	50.7
A5	8	0	203800	0.32	290	406	0.20	0.33	1.40	58.4
		45	201900	0.30	289	409	0.18	0.31	1.42	52.4
		90	199000	0.28	281	403	0.18	0.29	1.43	52.9
	3	90	213800	0.30	361	467	0.13	0.27	1.30	36.0

435 **Table 10** Effective material properties of as-built coupons of 8 mm nominal thickness.

Coupon	E (MPa)	v	f_y (MPa)	f_u (MPa)	ε_u	ε_f	f_u/f_y	$\varepsilon_u/\varepsilon_y$
A1-8-0-1	199400	0.29	300	424	0.21	0.38	1.41	61.2
A1-8-0-2	218600	0.25	342	452	0.17	0.28	1.32	47.3
A1-8-0-3	202200	0.28	309	428	0.20	0.36	1.39	55.8
A1-8-30-1	193900	0.29	280	394	0.16	0.30	1.41	45.2
A1-8-30-2	205100	0.30	285	407	0.15	0.26	1.43	45.2
A1-8-30-3	200200	0.27	290	414	0.19	0.37	1.43	54.6
A1-8-45-1	190400	0.29	282	392	0.17	0.29	1.39	48.1
A1-8-45-2	188900	0.25	276	386	0.14	0.24	1.40	40.5
A1-8-45-3	202900	0.26	295	418	0.19	0.35	1.42	54.5
A1-8-60-1	199600	0.28	288	409	0.14	0.25	1.42	40.4
A1-8-60-2	201100	0.30	275	388	0.12	0.21	1.41	36.9
A1-8-60-3	189200	0.29	281	395	0.14	0.24	1.41	41.5
A1-8-90-1	165700	0.26	272	393	0.16	0.24	1.44	43.3
A1-8-90-2	191500	0.29	276	391	0.14	0.23	1.42	40.4
A1-8-90-3	202200	0.28	283	398	0.14	0.22	1.41	41.5
A1-8-90-4	194400	0.29	284	399	0.15	0.24	1.41	43.2
A3-8-0-1	210900	0.27	302	413	0.22	0.35	1.37	64.3
A3-8-0-2	203000	0.29	300	416	0.21	0.34	1.39	59.3
A3-8-0-3	206400	0.26	303	419	0.21	0.33	1.38	60.4
A3-8-0-4	206600	0.29	312	428	0.21	0.33	1.37	58.9
A3-8-45-1	195800	0.26	283	404	0.19	0.34	1.43	53.8
A3-8-45-2	194800	0.27	279	403	0.17	0.28	1.44	50.2
A3-8-45-3	195100	0.27	281	405	0.19	0.34	1.44	55.2
A3-8-90-1	190500	0.24	273	396	0.15	0.21	1.45	44.6
A3-8-90-2	192700	0.25	275	397	0.16	0.22	1.44	45.2
A3-8-90-3	196400	0.26	284	405	0.17	0.24	1.43	47.9
A3-8-90-4	194200	0.27	282	403	0.16	0.24	1.43	46.8
A4-8-90-1	196700	0.25	283	406	0.18	0.26	1.43	51.3
A4-8-90-2	203900	0.27	282	402	0.16	0.25	1.43	48.4
A4-8-90-3	188500	0.28	283	408	0.19	0.32	1.44	53.3
A4-8-90-4	207500	0.31	275	403	0.17	0.30	1.47	49.8
A5-8-0-1	216900	0.36	306	423	0.20	0.35	1.38	58.4
A5-8-0-2	198300	0.29	285	409	0.21	0.31	1.43	60.3
A5-8-0-3	196200	0.30	278	386	0.19	0.33	1.39	56.6
A5-8-45-1	200700	0.27	289	406	0.17	0.28	1.41	49.9
A5-8-45-2	205500	0.31	283	401	0.18	0.34	1.42	52.7
A5-8-45-3	199600	0.34	296	421	0.19	0.31	1.42	54.6

A5-8-90-1	201400	0.25	279	401	0.18	0.29	1.44	52.7
A5-8-90-2	197300	0.27	278	400	0.18	0.29	1.44	51.9
A5-8-90-3	196200	0.30	282	403	0.18	0.29	1.43	53.2
A5-8-90-4	200900	0.29	286	407	0.18	0.29	1.43	53.8

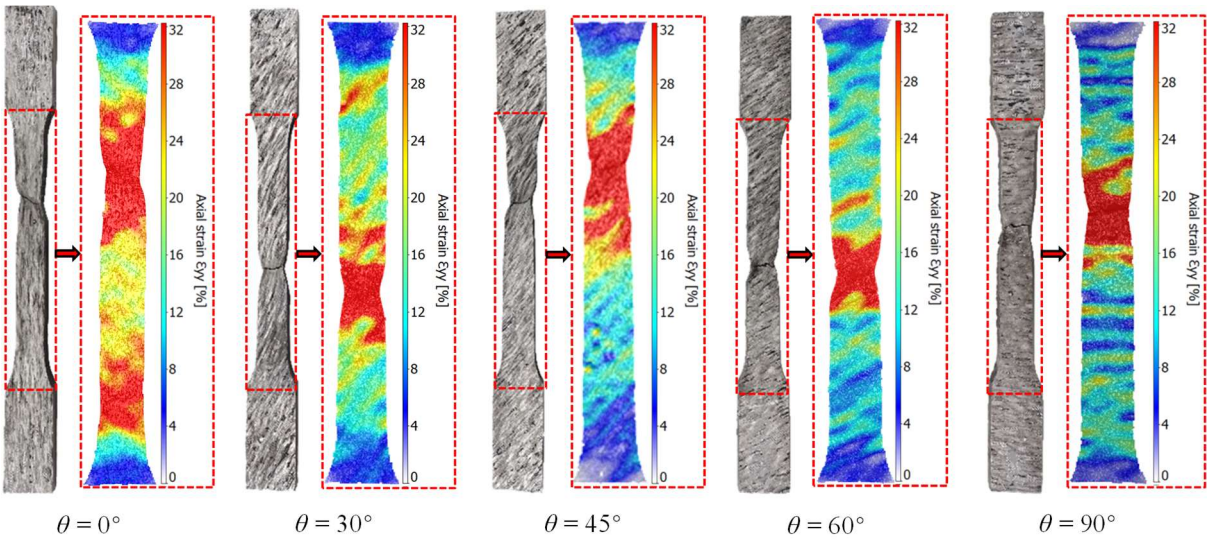


Fig. 26. Typical t_{nom} = 8 mm as-built normal-strength steel coupons after fracture, with DIC axial strain plots at fracture.

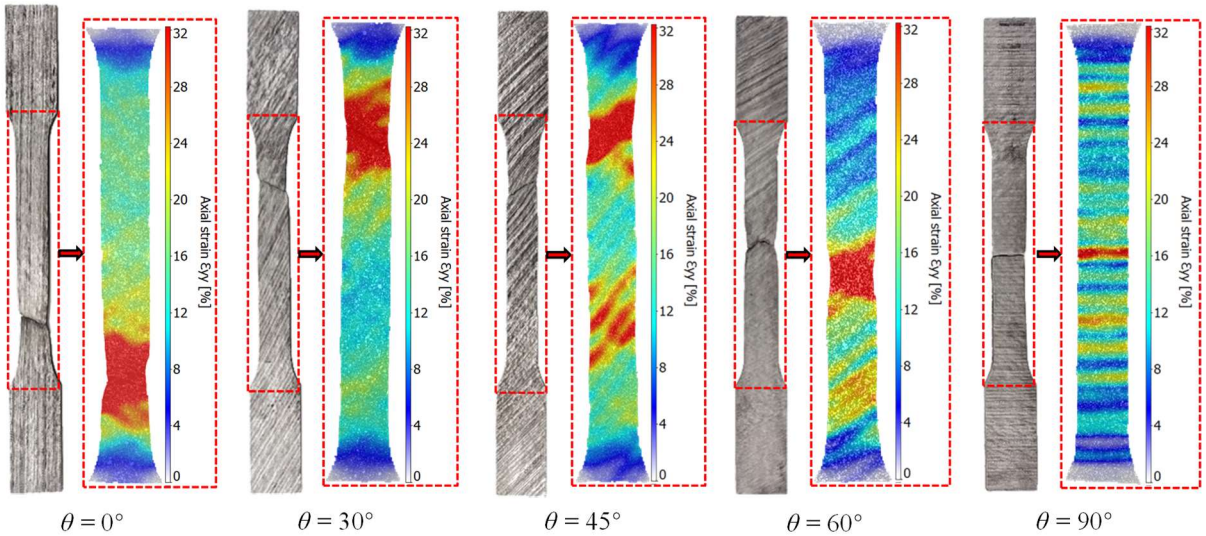


Fig. 27. Typical t_{nom} = 3 mm as-built normal-strength steel coupons after fracture, with DIC axial strain plots at fracture.

444 **Table 11** Effective material properties of as-built coupons of 3 mm nominal thickness.

Coupon	E (MPa)	v	f_y (MPa)	f_u (MPa)	ε_u	ε_f	f_u/f_y	$\varepsilon_u/\varepsilon_y$
A1-3-0-1	210600	0.29	388	486	0.17	0.33	1.25	43.7
A1-3-0-2	217700	0.27	388	481	0.18	0.34	1.24	47.7
A1-3-0-3	212800	0.27	383	485	0.17	0.36	1.27	45.1
A1-3-30-1	208200	0.27	372	478	0.15	0.38	1.29	40.2
A1-3-30-2	214300	0.24	389	495	0.15	0.34	1.27	39.8
A1-3-30-3	222800	0.23	373	478	0.15	0.39	1.28	41.0
A1-3-45-1	199900	0.27	366	479	0.17	0.27	1.31	44.2
A1-3-45-2	217100	0.28	384	485	0.15	0.28	1.26	39.2
A1-3-45-3	208700	0.26	362	464	0.12	0.30	1.28	31.7
A1-3-60-1	204800	0.28	354	457	0.13	0.28	1.29	35.7
A1-3-60-2	214800	0.28	371	475	0.14	0.32	1.28	36.5
A1-3-60-3	208400	0.28	361	470	0.13	0.23	1.30	35.2
A1-3-90-1	203100	0.28	341	464	0.13	0.20	1.36	36.5
A1-3-90-2	205000	0.28	348	460	0.14	0.22	1.32	36.9
A1-3-90-3	194800	0.32	336	`446	0.12	0.23	1.33	33.1
A1-3-90-4	201800	0.27	354	460	0.13	0.17	1.30	33.7
A2-3-0-1	217800	0.27	580	659	0.06	0.15	1.14	12.2
A2-3-0-2	216400	0.27	617	689	0.07	0.13	1.12	13.8
A2-3-0-3	220800	0.28	671	731	0.08	0.20	1.09	15.8
A2-3-30-1	217100	0.28	563	655	0.06	0.21	1.16	12.3
A2-3-30-2	224100	0.26	574	672	0.08	0.19	1.17	17.5
A2-3-30-3	215200	0.30	577	668	0.06	0.14	1.16	12.7
A2-3-45-1	215600	0.29	552	654	0.06	0.14	1.18	13.8
A2-3-45-2	219300	0.26	565	668	0.08	0.17	1.18	17.7
A2-3-45-3	217200	0.29	563	665	0.07	0.15	1.18	15.5
A2-3-60-1	215800	0.27	540	650	0.06	0.15	1.20	13.9
A2-3-60-2	204500	0.25	514	614	0.06	0.11	1.19	12.4
A2-3-60-3	216300	0.30	553	647	0.06	0.13	1.17	12.3
A2-3-90-1	221800	0.28	545	640	0.06	0.12	1.18	13.0
A2-3-90-2	222800	0.28	562	656	0.06	0.13	1.17	12.8
A2-3-90-3	217400	0.29	541	647	0.07	0.14	1.20	14.8
A2-3-90-4	188000	0.24	566	669	0.07	0.13	1.18	13.0
A2-3-90-5	208900	0.28	538	643	0.06	0.11	1.20	13.8
A5-3-90-1	212400	0.29	353	470	0.14	0.22	1.33	37.4
A5-3-90-1	217000	0.31	360	465	0.13	0.26	1.29	35.9
A5-3-90-1	212300	0.32	359	462	0.13	0.29	1.29	34.5
A5-3-90-1	213400	0.30	371	473	0.14	0.28	1.28	36.2

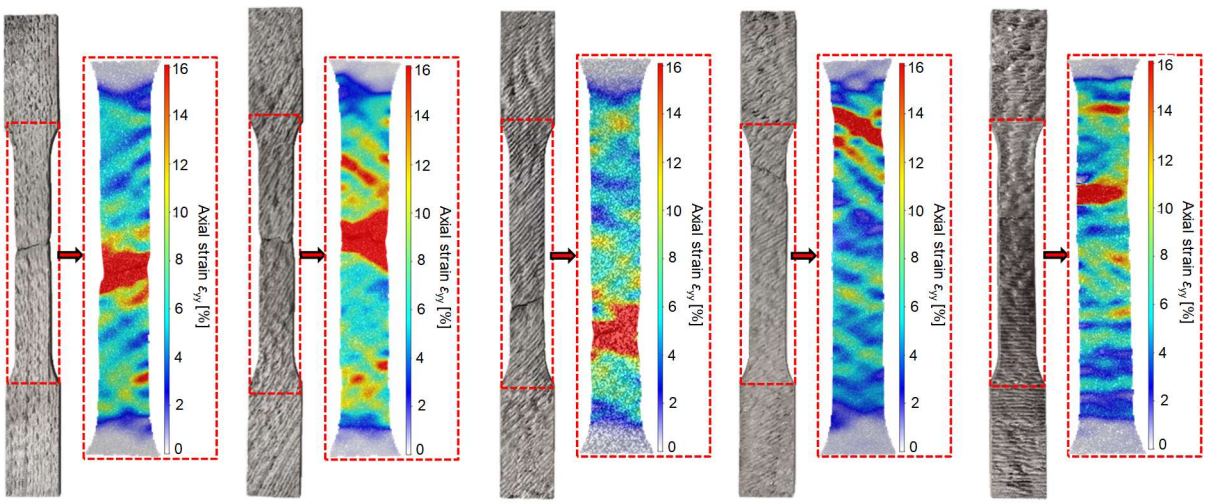


Fig. 28. Typical t_{nom} = 3 mm as-built high-strength steel coupons after fracture, with DIC axial strain plots at fracture.

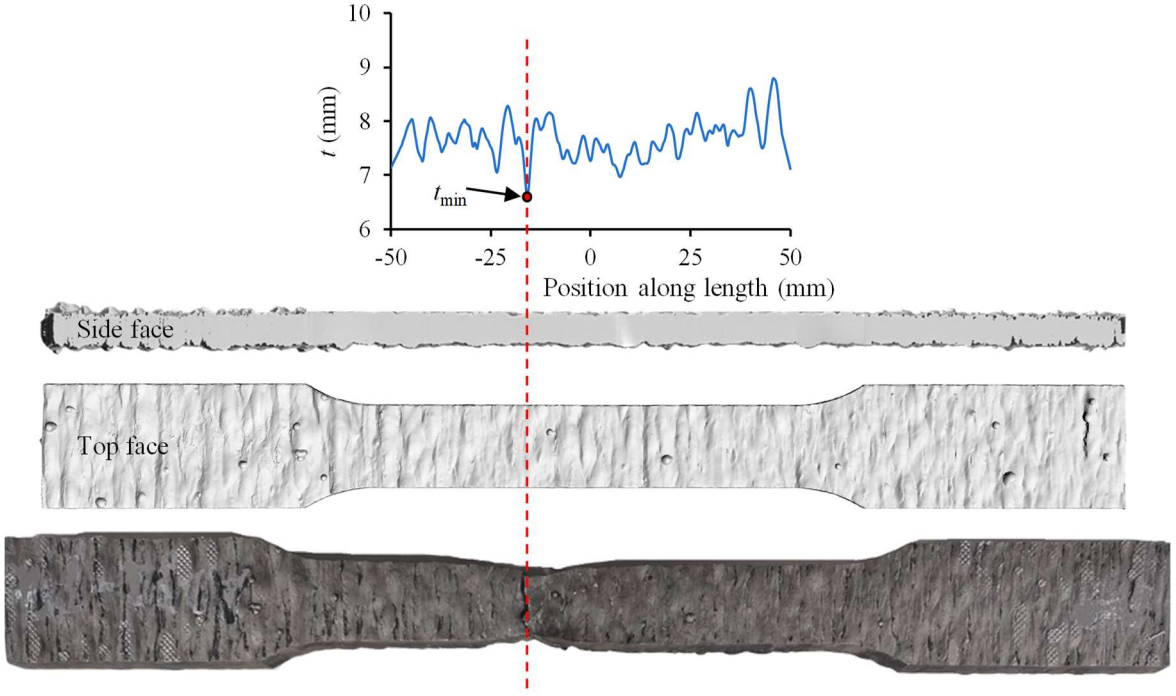


Fig. 29. Typical as-built coupon fractured at the cross-section of minimum average thickness t_{min}.

4.2.4 Comparison with properties of as-welded material from manufacturer

The strength and ductility of the tested WAAM materials are compared with the as-welded properties reported by the manufacturer in Table 12, with the average mechanical properties (i.e. f_y, f_u and ε_f in Tables 6 and 9) normalised by the corresponding manufacturer's measurements on as-welded material (i.e. $f_{y,aw}$, $f_{y,aw}$ and $\varepsilon_{f,aw}$, respectively, as reported in Table 2). It is shown that the WAAM materials generally exhibited higher ductility but lower strength

compared to the conventional welds examined by the manufacturer. The observed higher ductility is due to the slower cooling rates and repeated thermal cycles experienced by the deposited material during manufacture, similar to the tempering effect [22,28]. Compared to conventional welding processes, the WAAM process typically features slower heat dissipation, more heat accumulation and hence slower cooling rates, which are reflected by the longer cooling times $t_{8/5}$, as discussed in Section 4.3. The cooling rate does of course depend on the welding process, welding strategy and part geometry, so still vary from case to case. The lower strength observed for the as-built coupons is also attributed to the slower cooling rates associated with the WAAM process relative to conventional welding processes, together with the weakening effect of the as-built geometric undulations. For the machined coupons, on the other hand, the geometric undulations were removed, which enabled the influence of the slower cooling rates to be isolated; on average, relative to the as-welded values provided by the manufacturer, the measured yield and ultimate strengths were both about 30% and 20% lower for the t_{nom} = 8 mm and 3 mm normal-strength steel coupons, respectively, and less than 5% lower for the t_{nom} = 3 mm high-strength steel coupons. In addition to the more rapid cooling rate of the as-welded (compared to the WAAM) material, the higher strength values provided by the manufacturer may also be partly due to the higher strain rates typically employed by manufacturers in tensile testing. More detailed insight into the influence of the cooling rate and as-built geometry on the resulting mechanical properties is provided in the next two subsections.

Table 12 Average strength and ductility of tested WAAM material relative to corresponding as-welded properties reported by the manufacturer.

Material	t_{nom} (mm)	Surface	$f_y/f_{y,aw}$	$f_u/f_{u,aw}$	$\varepsilon_f/\varepsilon_{f,aw}$
Normal-strength steel	8	As-built	0.63	0.72	1.29
		Machined	0.66	0.73	1.48
	3	As-built	0.78	0.82	1.16
		Machined	0.83	0.83	1.27
High-strength steel	3	As-built	0.77	0.83	0.82
		Machined	0.95	0.99	1.39

4.3 Influence of cooling rate on the mechanical properties

The cooling rate is regarded as a critical factor influencing the material properties of welded steels [27,42], and it is well known that slower cooling leads to coarser grains and lower mechanical strength [28,43]. The cooling time from 800 °C to 500 °C, termed the $t_{8/5}$ time, is a typical parameter used to characterise the cooling rate, since this is the temperature interval in which the most important microstructural changes occur in steels. It has been shown that increasing the $t_{8/5}$ time can result in decreasing strengths in welded steels [44,45]. Hence, the $t_{8/5}$ time is adopted herein to explain the observed strengths of the WAAM plates. According to EN 1011-2 [46], the $t_{8/5}$ time for two-dimensional (i.e. applicable to sheets and thin plates) heat dissipation can be determined from:

$$t_{8/5} = \frac{Q^2}{4\pi\lambda\rho t^2}\left(\frac{1}{(500-T_\mathrm{p})^2} - \frac{1}{(800-T_\mathrm{p})^2}\right) \quad (1)$$

where λ is the thermal conductivity, ρ is the density, t is the plate thickness and T_p is the preheat temperature, i.e. the initial plate temperature T_0 for the first deposition layer and the interpass temperature T_i for subsequent layers. It can be seen from Eq (1) that the $t_{8/5}$ time increases with the square of the heat input Q and the interpass temperature T_i, but is inversely proportional to the square of the plate thickness t. The heat input, Q, is determined using:

$$Q = \varepsilon E = \varepsilon U(I/V) \quad (2)$$

where E is the energy input and ε is the thermal efficiency of the welding process, taken as 0.8 for MIG welding. The parameters U, I and V are the arc voltage, arc current and travel speed, respectively, as given in Table 3.

The interpass temperature was not explicitly measured in the present study, but given that the examined WAAM plates were deposited with a constant inter-layer dwell time of 30 s, the interpass temperature progression can be assumed to follow the trend shown in Fig. 30, where the evolution of T_i during a similar WAAM process with an inter-layer dwell time of 36 s is presented [47]. It can be seen that T_i increases with the successive deposition of layers, but at a decreasing growth rate, and tends to level off at just over 200 °C, which is below the maximum allowable interpass temperature (typically 250-350 °C) specified in EN 1011-2 [46].

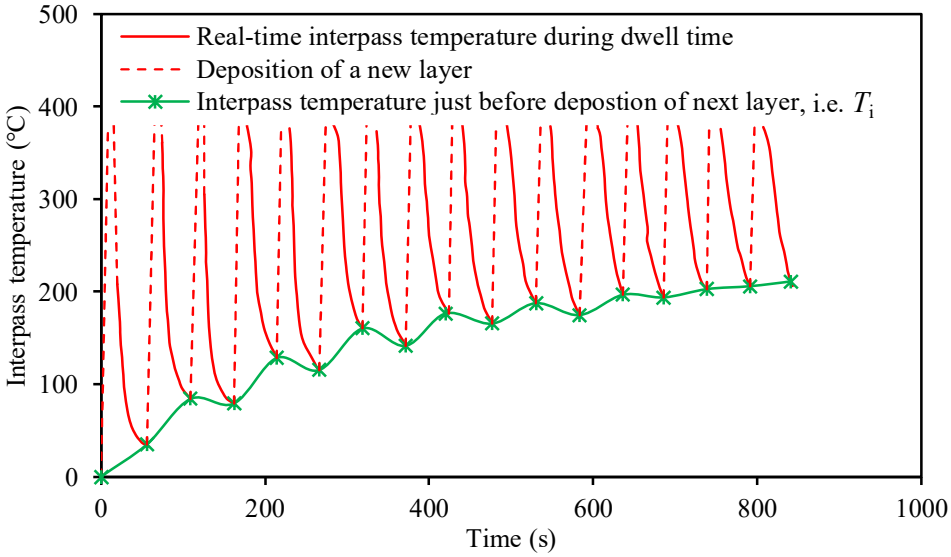


Fig. 30. Variation of interpass temperature during WAAM with a constant dwell time, adapted from [47].

The tensile test results showed that the strengths exhibited by some $\theta = 0°$ coupons were almost equal to the measured values stated by the manufacturer, and higher than those displayed by the coupons extracted in the other directions. This is attributed to a number of the $\theta = 0°$ coupons being extracted from the bottom region of the WAAM plates (i.e. close to the base/build plate), where the lower interpass temperatures, as indicated in Fig. 30, would have led to shorter $t_{8/5}$ times and hence higher mechanical strengths, compared to the coupons extracted elsewhere. Further, the tensile tests revealed lower strengths for the thicker material ($t_{nom} = 8$ mm) compared to the thinner material ($t_{nom} = 3$ mm), which can also be explained with reference to their different cooling times. Using Eq. (2), the heat input Q is calculated to be 322 J/mm and 80 J/mm for the thick and thin plates, respectively. Substitution of the obtained heat input Q and the plate thickness t into Eq. (1) indicates a longer $t_{8/5}$ time for the thicker material, resulting in the lower strength relative to the thinner material.

4.4 Influence of as-built geometry on the mechanical properties

The influence of the undulating as-built geometry on the resulting mechanical properties was quantified by making comparisons between the results of the as-built and machined coupon

529 tests, as presented in Fig. 31 and Table 13, where the effective material properties of the as-
530 built coupons are denoted using the subscript "eff". As expected, the machined coupons
531 generally exhibited superior mechanical properties compared to the as-built coupons, with the
532 exception of some prematurely fractured coupons, as described in Section 4.2.2, and some 0°
533 and 30° coupons that were influenced by location-related higher cooling rates, as mentioned in
534 Section 4.3. Note that, the premature fracture of the machined coupons A1-3-60-2M and A1-
535 3-60-3M led to increased ratios of $\varepsilon_{u,eff}/\varepsilon_u$ and $\varepsilon_{f,eff}/\varepsilon_f$ – see Fig. 31(e) and 31(f), which would
536 otherwise have been equal to 0.82 and 0.90 respectively if these two coupons had been
537 excluded from the analysis. For all plate types, the negative influence of the undulating as-built
538 geometry was most significant for the 90° coupons, with reductions, relative to the machined
539 coupon results, of up to about 10% for E, f_y and f_u, and 40% for ε_u and ε_f; no obvious effect of
540 the geometric undulations on the Poisson's ratios was observed. Overall, the ratios of the
541 mechanical properties (i.e. E_{eff}/E, ν_{eff}/ν, $f_{y,eff}/f_y$, $f_{u,eff}/f_u$, $\varepsilon_{u,eff}/\varepsilon_u$ and $\varepsilon_{f,eff}/\varepsilon_f$) tended to decrease
542 with increasing θ, owing to the increasing geometric variability, expressed as A_{sd}/A.

543 **Table 13** Comparison of average material properties between as-built and machined coupons.

Plate type	t_{nom} (mm)	θ (°)	E_{eff}/E	ν_{eff}/ν	$f_{y,eff}/f_y$	$f_{u,eff}/f_u$	$\varepsilon_{u,eff}/\varepsilon_u$	$\varepsilon_{f,eff}/\varepsilon_f$
A1	8	0	1.03	0.97	1.02	1.02	0.91	0.88
		30	1.00	0.96	0.92	0.95	0.80	0.82
		45	0.97	1.05	0.89	0.94	0.80	0.79
		60	0.96	1.06	0.90	0.95	0.70	0.67
		90	0.92	0.96	0.91	0.94	0.85	0.75
	3	0	1.01	1.07	0.99	0.99	0.92	0.90
		30	1.01	0.87	0.98	1.00	0.95	1.06
		45	0.94	0.95	0.95	0.99	1.02	0.88
		60	0.99	1.14	0.91	1.02	1.37	1.33
		90	0.93	0.99	0.88	0.94	0.77	0.61
A2	3	0	0.99	1.00	0.96	0.97	0.80	0.72
		45	0.97	1.00	0.93	0.95	0.78	0.65
		90	0.96	0.97	0.92	0.95	0.71	0.60
A3	8	0	1.01	1.08	1.00	0.99	0.93	0.77
		45	0.90	0.94	0.89	0.95	0.94	0.90
		90	0.91	0.85	0.90	0.96	0.75	0.60
A4	8	90	1.01	0.94	0.93	0.95	0.88	0.84
A5	8	0	0.99	1.13	0.94	0.96	0.91	0.78

45	0.97	1.07	0.94	0.99	0.89	0.82
90	0.97	1.07	0.92	0.97	0.94	0.85

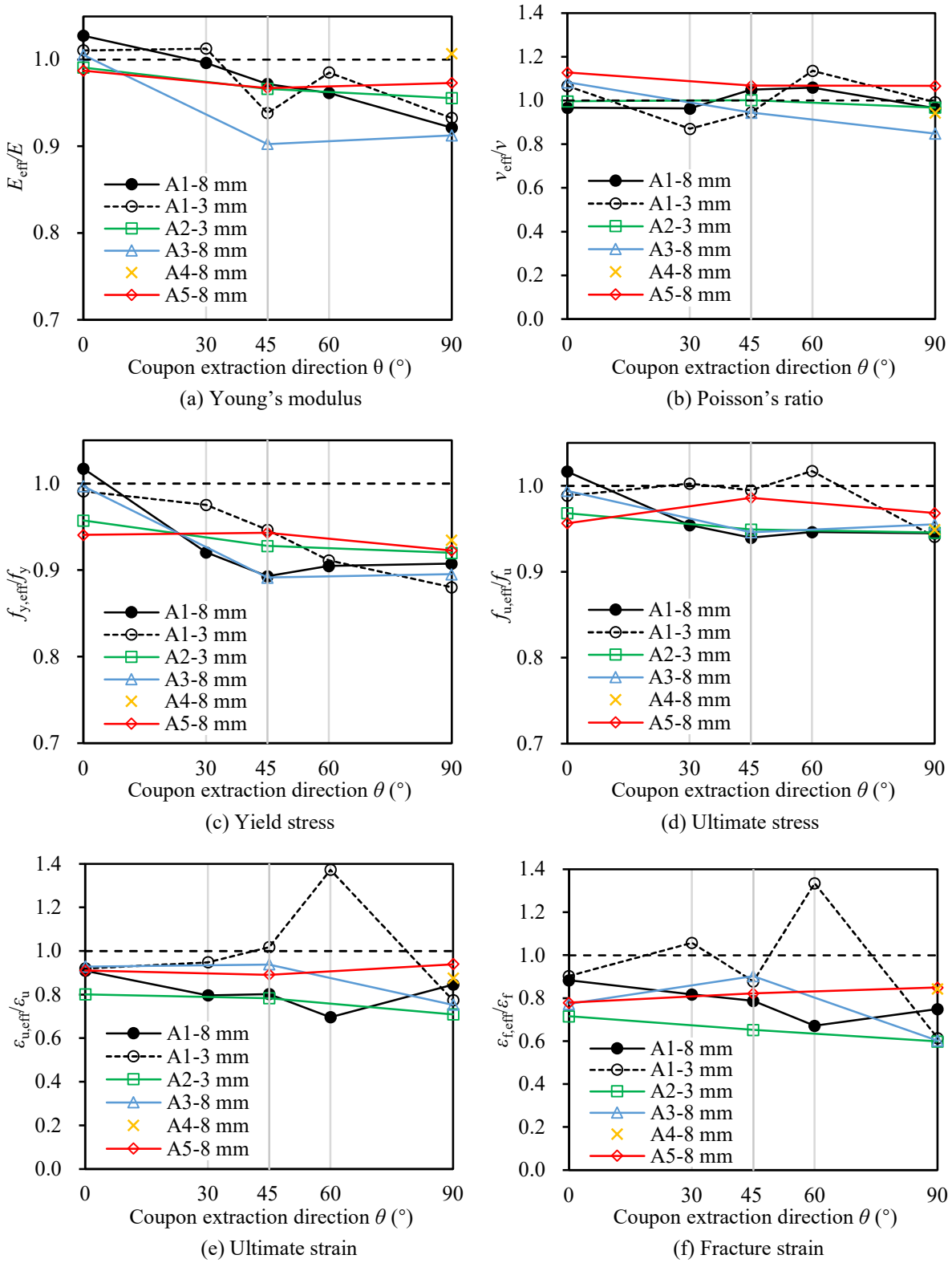


Fig. 31. Comparison of key mechanical properties between as-built and machined coupons.

4.5 Influence of deposition strategy on the mechanical properties

The influence of the employed deposition strategy on the mechanical properties of the WAAM materials is discussed in this section. Table 14 presents the average material properties of plate types A3, A4 and A5 normalised by the equivalent average properties of plate type A1 (denoted E_{A1}, ν_{A1}, $f_{y,A1}$, $f_{u,A1}$, $\varepsilon_{u,A1}$, and $\varepsilon_{f,A1}$), while the normalised (for the same coupon extraction direction) material parameters of the individual coupon specimens are plotted against their respective geometric variability A_{sd}/A normalised by the variability of the corresponding coupons of plate type A1 $A_{sd,A1}/A_{A1}$ in Fig. 32. Note that plate type A1 was built using the current default WAAM deposition strategy [8], and thus the resulting mechanical properties and geometric variability are selected as the benchmark for the conducted comparisons.

Table 14 Comparison of average material properties among different deposition strategies.

Plate type/deposition strategy	Surface	E/E_{A1}	ν/ν_{A1}	$f_y/f_{y,A1}$	$f_u/f_{u,A1}$	$\varepsilon_u/\varepsilon_{u,A1}$	$\varepsilon_f/\varepsilon_{f,A1}$
A3	As-built	1.01	0.97	0.98	1.00	1.09	1.01
	Machined	1.05	1.01	0.99	1.00	1.08	1.09
A4	As-built	1.06	0.99	1.01	1.02	1.18	1.20
	Machined	0.97	1.02	0.98	1.02	1.14	1.06
A5	As-built	1.04	1.08	1.00	1.00	1.10	1.16
	Machined	1.02	1.00	0.98	0.99	1.04	1.07

As can be seen from Table 14, the average mechanical properties obtained from both as-built and machined coupons were relatively insensitive to changes in the deposition strategy. The influence of the deposition strategy on the resulting mechanical properties, as well as on the geometric variability, is further demonstrated in Fig. 32. It is apparent that the employed deposition strategies led to differences in the geometric variability of the WAAM plates, with deposition strategies A1 and A5 showing the maximum and minimum A_{sd}/A values, respectively; despite these differences, the variations in Young's modulus and strength remained within about ±10%. Ductility, was, as explained in Section 4.2, more sensitive to geometric variability due to the strain localisation effect associated with troughs in cross-sectional area – the effect of this can also be seen in Fig. 32, where the ultimate and fracture strain ratios ($\varepsilon_u/\varepsilon_{u,A1}$ and $\varepsilon_f/\varepsilon_{f,A1}$ respectively) are shown to generally decrease with increasing values of $A_{sd}/A/(A_{sd,A1}/A_{A1})$, with the downward trends being more pronounced than those of the ratios of E/E_{A1}, $f_y/f_{y,A1}$ and $f_u/f_{u,A1}$.

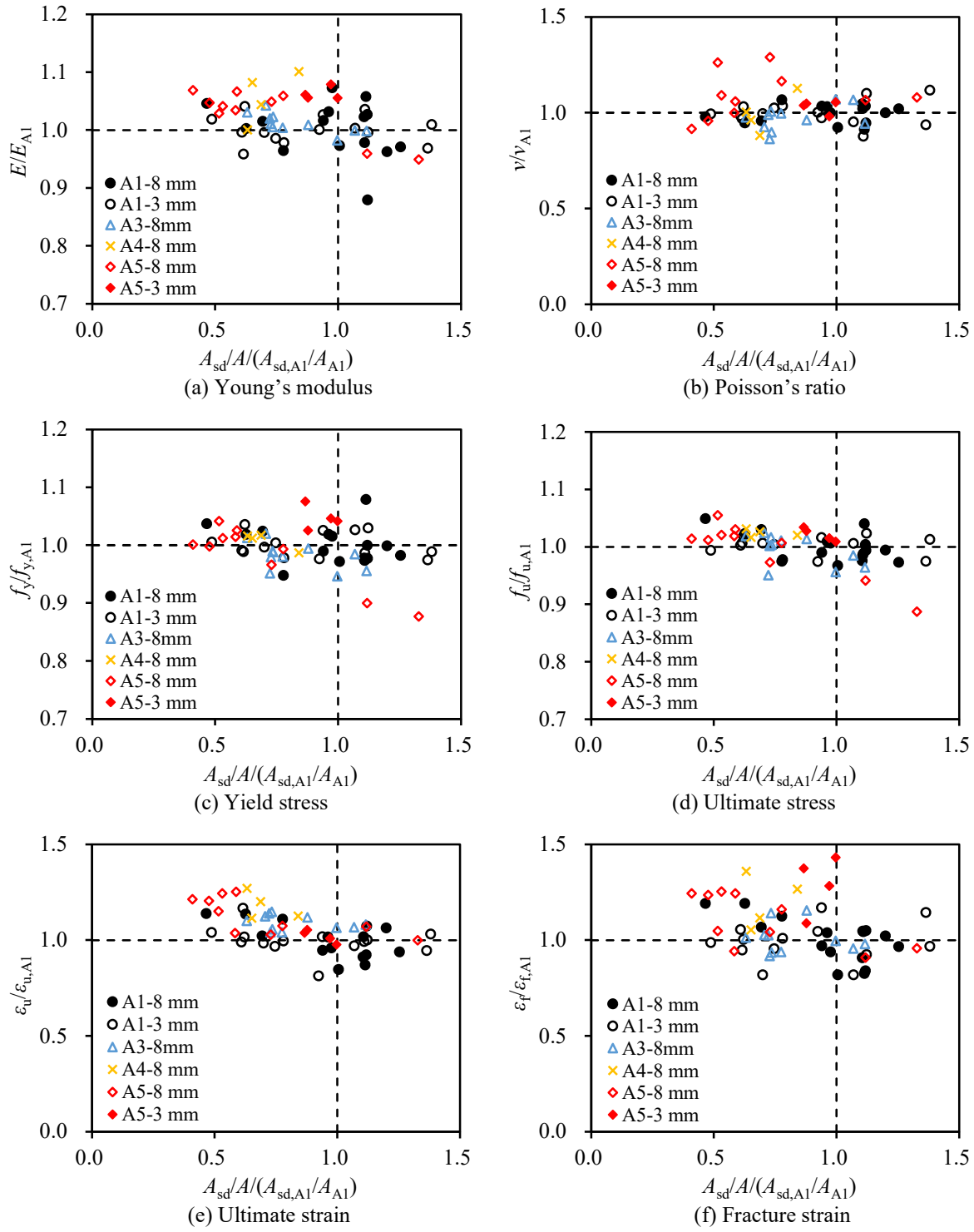


Fig. 32. Comparison of key mechanical properties among different deposition strategies.

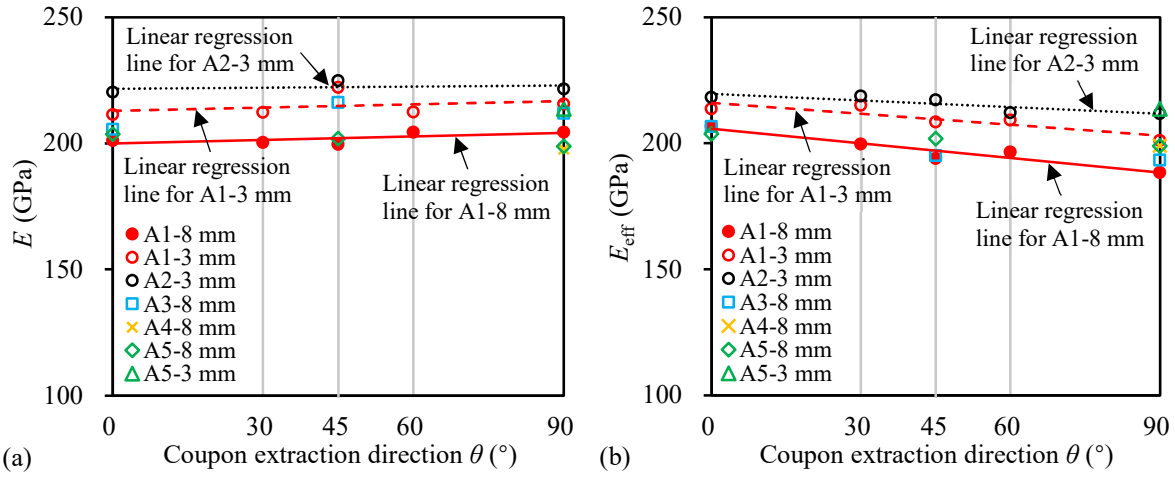
4.6 Material anisotropy

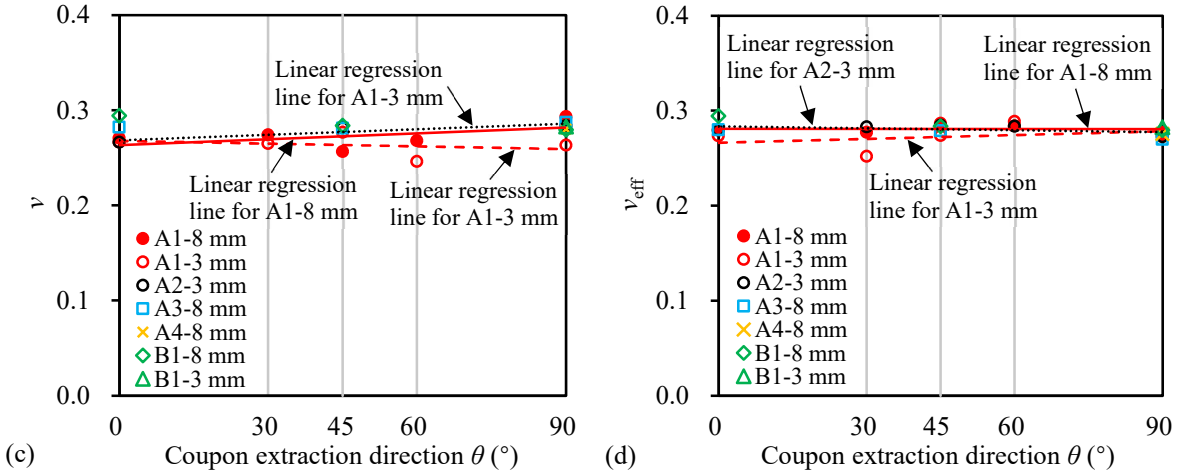
The anisotropy of the studied WAAM material is discussed in this section. The average mechanical properties of both the machined and as-built coupons (reported in Tables 6 and 9 respectively), grouped by plate type and nominal material thickness, are plotted against the

coupon extraction direction θ in Fig. 33; linear regression lines for the plates type A1 and type A2 are also plotted.

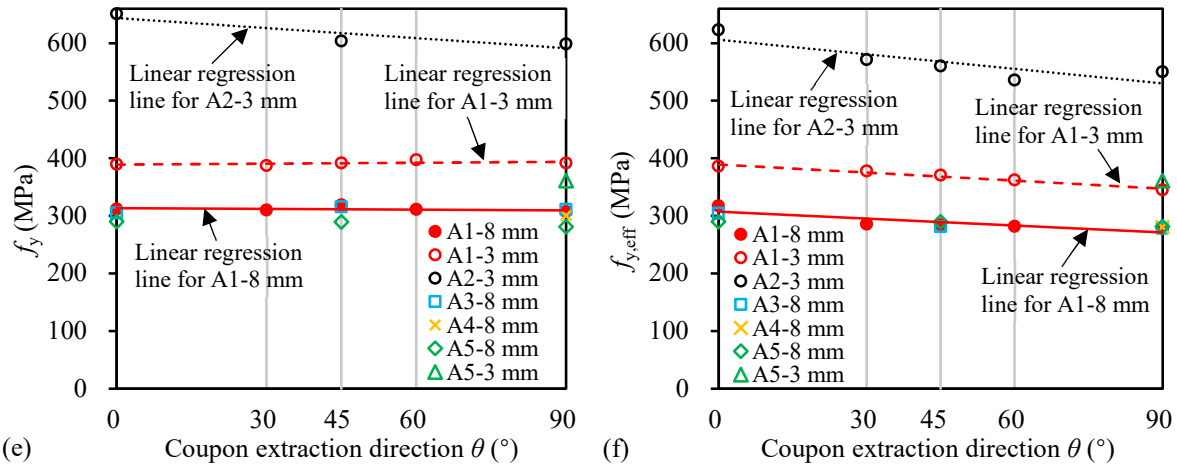
The anisotropy exhibited by the machined coupons was very mild, with almost consistent values of Young's modulus, yield strength and ultimate strength among the different coupon directions, as reflected by the nearly horizontal regression lines. It is worth noting that the ultimate and fracture strains (see Fig. 33 (i) and (k)) of the machined normal-strength steel coupons of plate type A1 appeared to decrease with increasing θ, while no such trend was observed for the machined high-strength steel coupons (plate type A2).

The as-built coupons displayed stronger, though still generally rather mild and partially geometrically-induced, anisotropy, with the effective mechanical properties (i.e. E_{eff}, $f_{\text{y,eff}}$, $f_{\text{u,eff}}$, $\varepsilon_{\text{u,eff}}$ and $\varepsilon_{\text{f,eff}}$) tending to decrease with increasing θ, with the ductility measures ($\varepsilon_{\text{u,eff}}$ and $\varepsilon_{\text{f,eff}}$) showing the greatest variation with θ, as indicated by the inclinations of the regression lines. Overall, the as-built coupons exhibited greater variation in effective mechanical properties than the machined coupons with varying extraction direction; this is attributed to the influence of the geometric undulations – see Fig. 34.

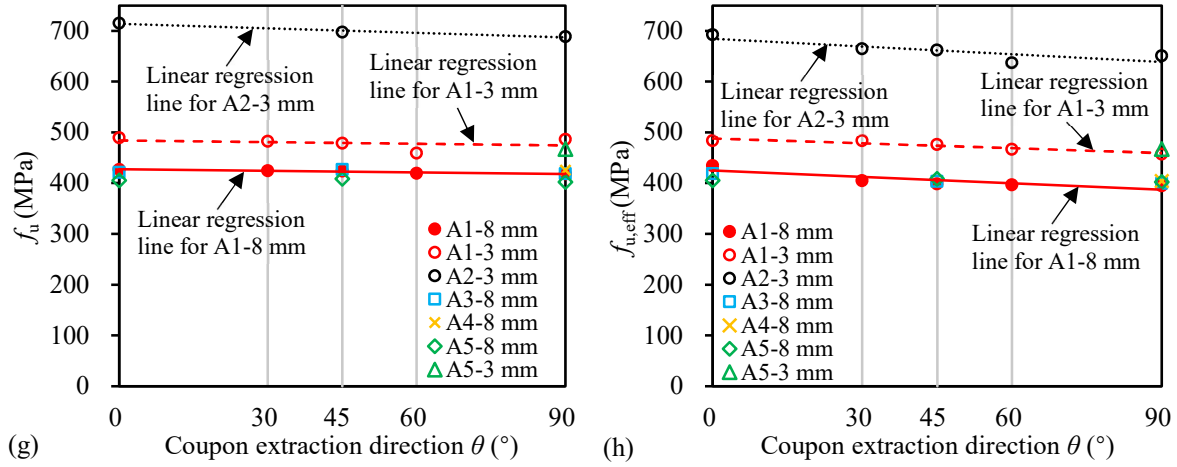



0.4
0.3
0.2
0.1
0.0
ν
Linear regression line for A1-3 mm
Linear regression line for A1-8 mm
Linear regression line for A1-3 mm
A1-8 mm
A1-3 mm
A2-3 mm
A3-8 mm
A4-8 mm
B1-8 mm
B1-3 mm
0
30
45
60
90
Coupon extraction direction θ (°)
(c)
0.4
0.3
0.2
0.1
0.0
ν_eff
Linear regression line for A2-3 mm
Linear regression line for A1-8 mm
Linear regression line for A1-3 mm
A1-8 mm
A1-3 mm
A2-3 mm
A3-8 mm
A4-8 mm
B1-8 mm
B1-3 mm
0
30
45
60
90
Coupon extraction direction θ (°)
(d)

604


600
500
400
300
200
100
0
f_y (MPa)
Linear regression line for A2-3 mm
Linear regression line for A1-3 mm
Linear regression line for A1-8 mm
A1-8 mm
A1-3 mm
A2-3 mm
A3-8 mm
A4-8 mm
A5-8 mm
A5-3 mm
0
30
45
60
90
Coupon extraction direction θ (°)
(e)
600
500
400
300
200
100
0
f_y,eff (MPa)
Linear regression line for A2-3 mm
Linear regression line for A1-3 mm
Linear regression line for A1-8 mm
A1-8 mm
A1-3 mm
A2-3 mm
A3-8 mm
A4-8 mm
A5-8 mm
A5-3 mm
0
30
45
60
90
Coupon extraction direction θ (°)
(f)

605


700
600
500
400
300
200
100
0
f_u (MPa)
Linear regression line for A2-3 mm
Linear regression line for A1-3 mm
Linear regression line for A1-8 mm
A1-8 mm
A1-3 mm
A2-3 mm
A3-8 mm
A4-8 mm
A5-8 mm
A5-3 mm
0
30
45
60
90
Coupon extraction direction θ (°)
(g)
700
600
500
400
300
200
100
0
f_u,eff (MPa)
Linear regression line for A2-3 mm
Linear regression line for A1-3 mm
Linear regression line for A1-8 mm
A1-8 mm
A1-3 mm
A2-3 mm
A3-8 mm
A4-8 mm
A5-8 mm
A5-3 mm
0
30
45
60
90
Coupon extraction direction θ (°)
(h)

606

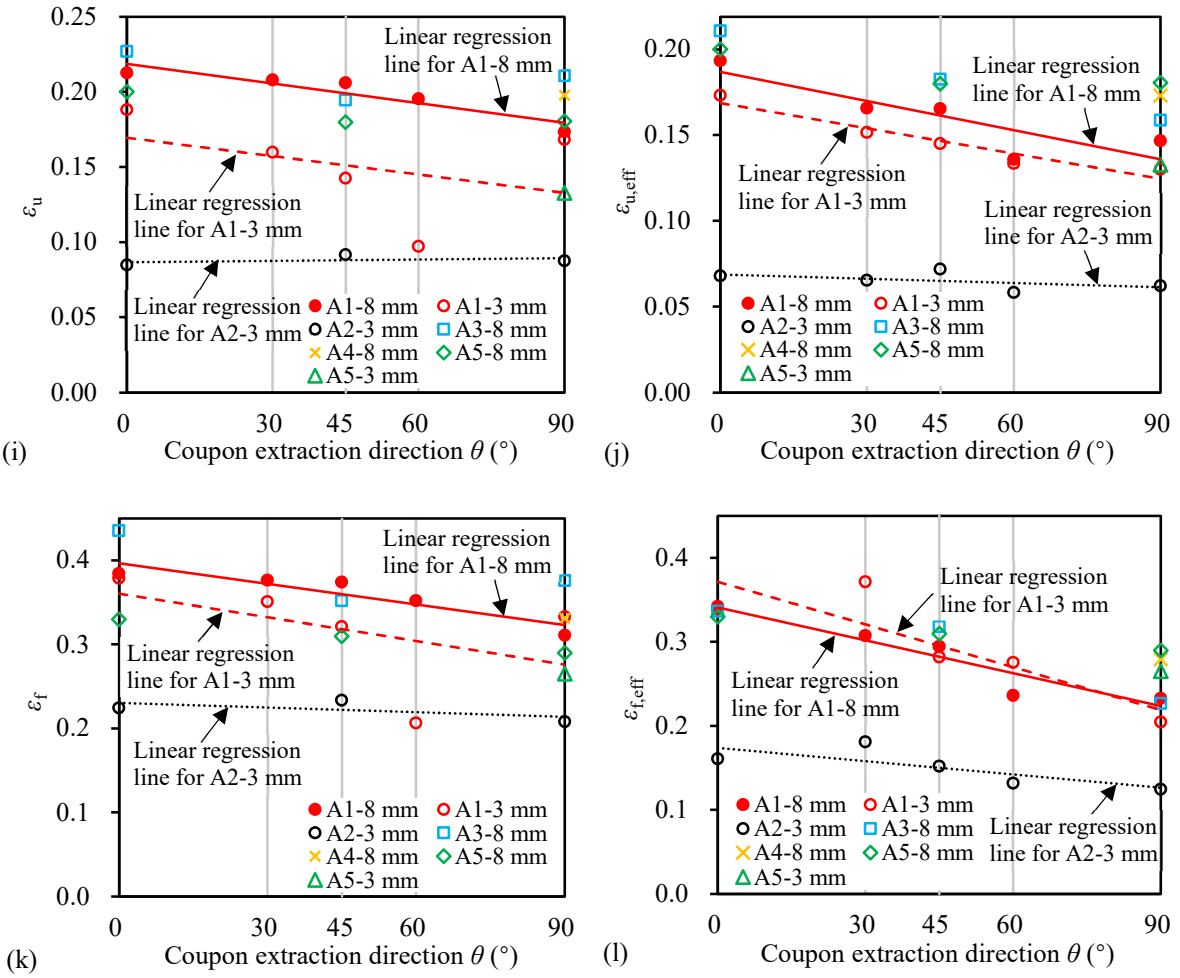


Fig. 33. Variation of key mechanical properties with coupon extraction direction for machined (left) and as-built (right) WAAM coupons.

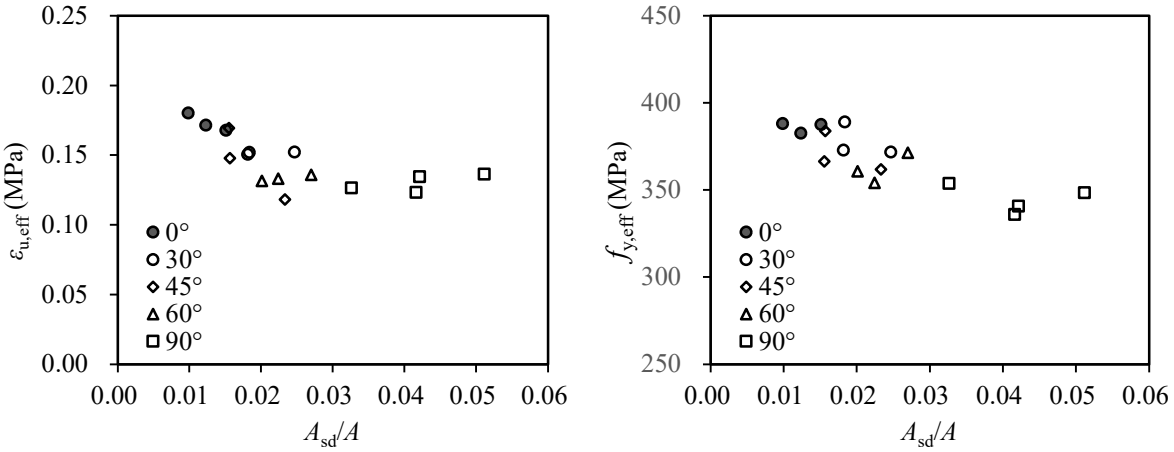


Fig. 34. Correlation of material strength and ductility with geometric variability, shown for t_{nom} = 3 mm coupons of plate type A1.

5 Microstructural characterisation

Microstructural characterisation was carried out on the studied WAAM material by means of optical microscopy (OM) and electron backscatter diffraction (EBSD), in order to assess the mechanical response from a metallurgical perspective. The microstructural testing was undertaken in the Engineering Alloys and Harvey Flowers EM Suite in the Department of Materials at Imperial College London.

5.1 Experimentation

To examine the microstructure of the printed material, metallographic samples, listed in Table 15, were extracted at different locations from the WAAM plates, with the axes LD, TD and ND being parallel, transverse and normal to the print layer direction, respectively – see Fig. 35. The metallographic samples were extracted away from the edges of the WAAM plates to avoid any influence from the plasma arc or water jet cutting on the examined microstructure. The sample labelling system begins with the plate type (i.e. A1-A5), followed by the nominal thickness of the plate in mm, the position on the height of the plate (i.e. T, M and B, representing the top, middle and bottom region of the plate respectively) and the normal to the examined surface (denoted by LD, TD and ND).

Table 15 Test samples for microstructural characterisation.

Sample	Optical Microscopy	EBSD/SEM
A1-3-T-LD/ND/TD	✓	
A1-3-M-LD/ND/TD	✓	✓
A1-3-B-LD/ND/TD	✓	
A1-3-B-LD	✓	✓
A1-3-B-ND	✓	
A1-3-B-TD	✓	
A2-3-B-LD/ND/TD	✓	✓
A3-8-M-LD	✓	✓
A4-8-M-LD	✓	✓
A5-8-M-LD	✓	✓

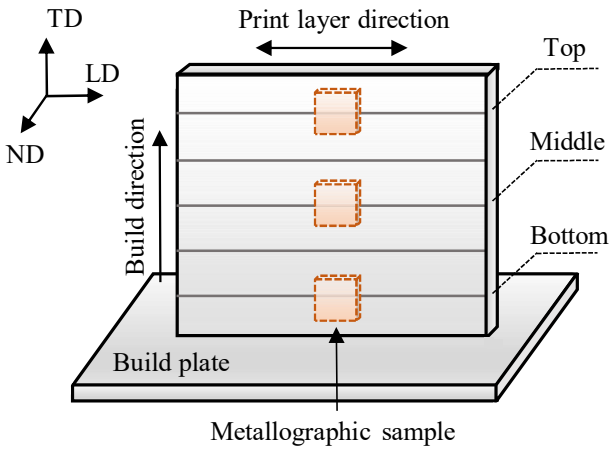


Fig. 35. Schematic illustration of extraction of metallographic samples.

The samples were prepared for metallographic examination in accordance with ASTM E3-11 [48]. One surface of each sample was ground with a series of silicon carbide abrasive papers up to 2000 grit, and polished to a mirror finish, sequentially using 3 µm and 1 µm diamond suspensions and a 0.04 µm diluted colloidal silica solution. The as-polished samples were then etched with a 3% Nital solution for 50 s to reveal their microstructure, and ultrasonically cleaned in acetone to remove any residual reagents. Finally, metallography was performed using an Olympus BX51 optical microscope.

Electron backscatter diffraction (EBSD) characterisation was also performed to gain deeper insight into the microstructure and crystallographic texture of the WAAM material. Since the quality of EBSD patterns is extremely sensitive to surface defects [49], all samples were prepared until the examined surfaces were free of visible scratches or contamination under an optical microscope. EBSD analyses were then performed using a Quanta FEG scanning electron microscope coupled with a Bruker eFlash HD EBSD detector, which was operated using a 20 kV electron beam acceleration voltage and with the samples tilted at 70° to the horizontal. During the EBSD measurements, large areas of 414 µm × 275 µm were sampled to capture a sufficient number of grains and hence enable a proper statistical description of the microstructure. The EBSD data were acquired and analysed using Esprit 2.3 [50], while the micrographs were post-processed for grain size measurements in ImageJ [51].

5.2 Results

5.2.1 Optical microscopy observations

Fig. 36 depicts typical optical micrographs of the normal- and high-strength WAAM steels, with all examined samples extracted from the bottom regions of the WAAM plates, and with

the examined surfaces normal to the LD direction (see Fig. 35). The microstructure of the t_{nom} = 8 mm material, shown in Fig. 36(a), comprised polygonal ferrite (PF) and intergranular lamellar pearlite (P), which is consistent with previous observations on WAAM mild steels [25,28,52,53]. Owing to the low carbon content of the feedstock material, only a low volume fraction of pearlite was observed, forming along the grain boundaries and triple junctions of the polygonal ferrite grains. A similar ferritic-pearlitic microstructure was observed for the t_{nom} = 3 mm material, as shown in Fig. 36(b), where a small content of acicular ferrite (AF) and bainite (B), often detected in WAAM mild steels [28,52,53], also formed due to the faster cooling rate of the thin plates compared to the thick plates. The WAAM high-strength steel displayed a mixture of acicular ferrite (AF), bainite (B) and martensite (M) phases, with the latter leading to the enhanced strength, but reduced ductility observed in the mechanical testing.

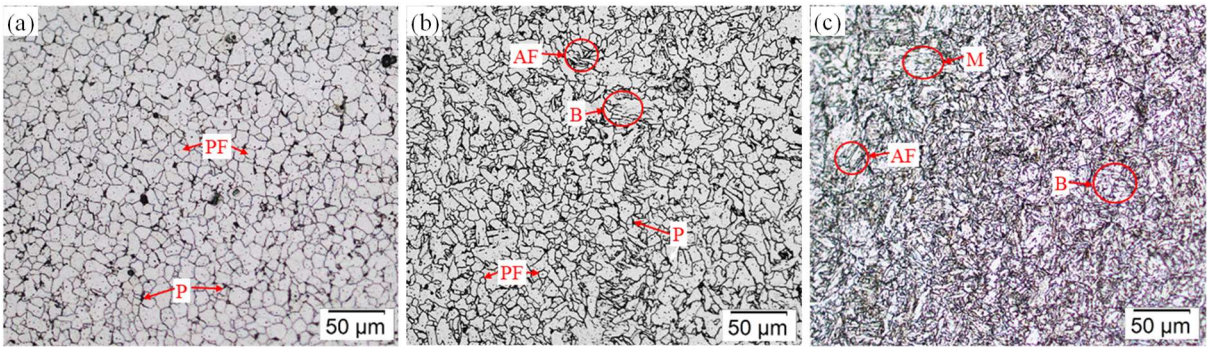


Fig. 36. Micrographs of metallographic samples: (a) A1-8-B-LD; (b) A1-3-B-LD; (c) A2-3-B-LD (PF: polygonal ferrite, AF: acicular ferrite, P: pearlite, B: bainite, M: martensite).

In addition to micro-constituents, grain size also has a significant influence on the mechanical properties of steels. Grain size analysis was therefore performed on the WAAM material based on the micrographs of Fig. 36. Owing to the slower cooling rate that promotes grain growth, the thicker normal-strength steel exhibited a larger grain size than the corresponding thinner material (12.1 μm versus 8.2 μm on average), leading to the lower measured mechanical strength, in line with the Hall-Petch relationship [54,55]. The high-strength steel revealed a microstructure with a finer grain size of 6.2 μm on average. Grain size is typically found to increase with increasing distance from the build plate; this is because of the slower cooling rates away from the build plate due to the reducing influence of the heatsink effect [22,26,56,57]. This finding was also confirmed herein by comparing the grain sizes of samples extracted from the top, middle and bottom regions of the t_{nom} = 8 mm WAAM plates (listed in Table 15), although the observed grain size variation was not significant.

The microstructure of the WAAM material was found to be largely insensitive to the employed deposition strategies, with the examined surfaces (A1-8-M-LD, A3-8-M-LD, A4-8-M-LD, A5-8-M-LD) showing similar grain morphologies, compositions and sizes. Further, micrographs taken from three orthogonal surfaces from both normal- and high-strength steel samples are presented in Fig. 37, indicating generally homogeneous and isotropic microstructures within the WAAM material.

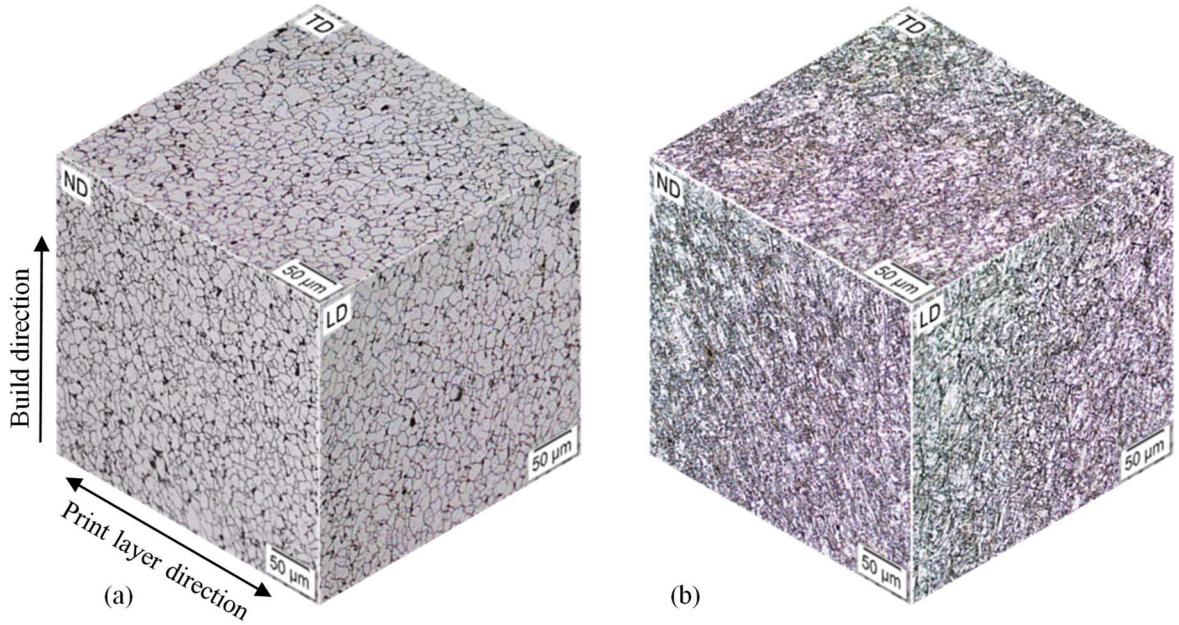
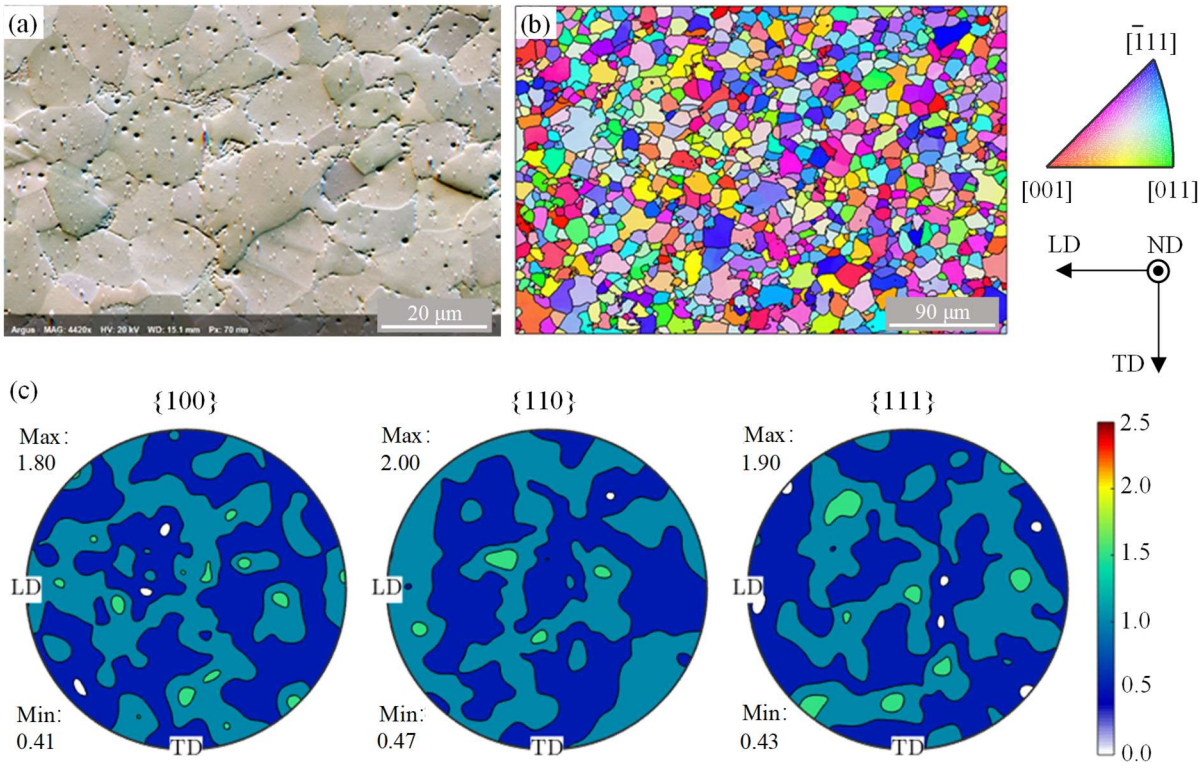


Fig. 37. Isometric micrographs of metallographic samples: (a) A1-8-T-TD/ND/LD; (b) A2-3-B-TD/ND/LD.

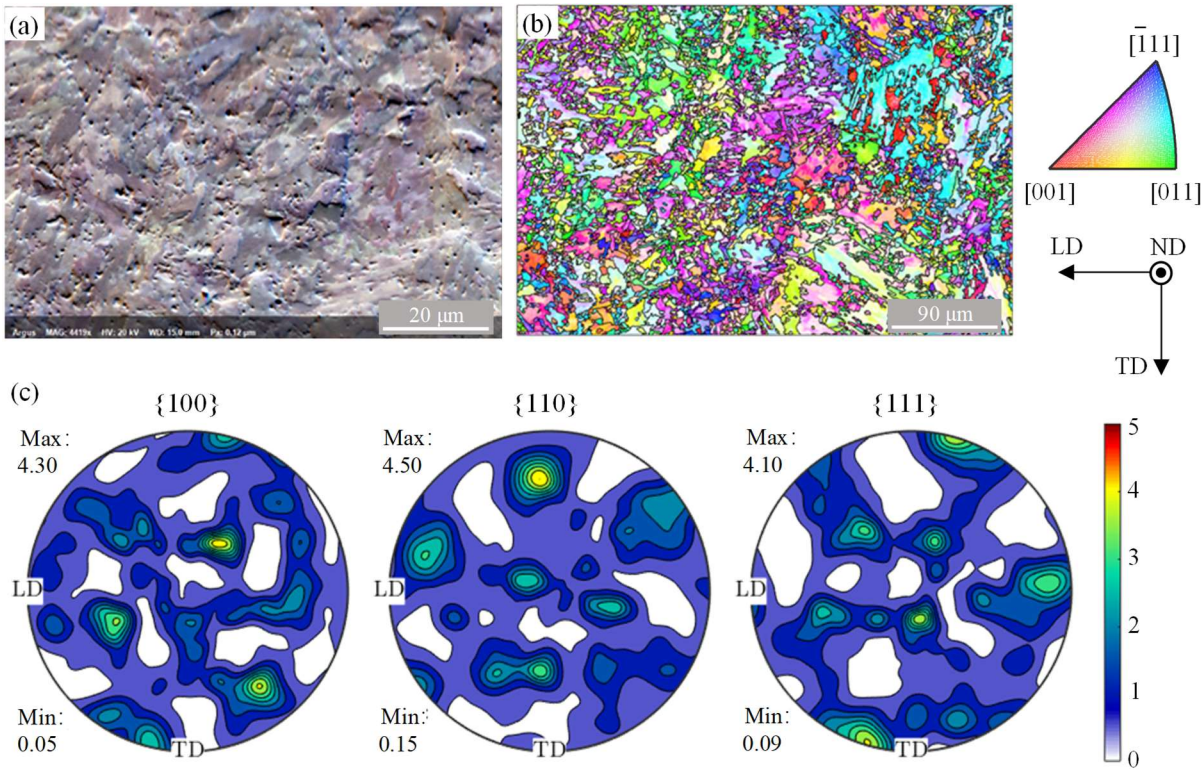
5.2.2 EBSD analysis

Forescatter diode (FSD) imaging was used during the EBSD analysis to visualise microstructural morphologies through diffraction contrast. Fig 38 shows a typical FSD image taken for a t_{nom} = 8 mm WAAM normal-strength steel sample, along with the corresponding inverse pole figure (IPF) map, where the colours indicate the crystal orientations. Randomly orientated equiaxed grains with an average grain size of 12.6 µm are revealed in the microstructure, which is in good agreement with the OM observations. Crystallographic data on 1562 grains were captured for the EBSD analysis, enabling a representative characterisation of the key microstructural features, including grain size and texture [58]. Typical {100}, {110} and {111} pole figures of the examined surface are shown in Fig. 38(c), where the plane of the pole figures is parallel to the examined surface, and the scale bar represents the texture intensity of specific crystallographic orientation distributions. The pole figures reveal a weak crystallographic texture, with an essentially random distribution of grain orientations.



704

705 **Fig. 38.** (a) FSD image; (b) inverse pole figure (with colours presented with respect to ND); (c) pole figures of
706 normal-strength steel sample A1-8-M-ND.



707

708 **Fig. 39.** (a) FSD image; (b) inverse pole figure (with colours presented with respect to ND); (c) pole figures of
709 high-strength steel sample A2-3-M-ND.

710

Fig. 39 depicts typical FSD and IPF maps of the WAAM high-strength steel, providing a vivid representation of the grain morphologies and orientations, where predominantly equiaxed grains can be observed. A total of 8511 grains were scanned during the EBSD measurements; the average grain size was 7.6 µm, much finer than that of the WAAM normal-strength steel. According to the pole figures in Fig. 39, the microstructure of the WAAM high-strength steel was also weakly textured, with no dominant crystallographic orientation. The observed absence of a strong crystallographic texture is consistent with previous studies on WAAM carbon steels [28,52,53,59]; previous studies on WAAM stainless steel have, on the other hand, revealed a strong crystallographic texture [12,13,37,60]. The reduced strength of the texture for this material is likely due to the large number of potential variants formed during the δ (BCC) → γ (FCC) → α (BCC) phase transformations.

Fig. 40 presents the phase maps of the WAAM normal- and high-strength steels. Both materials consist primarily of ferrite phase, while a fraction of austenite retained during solidification is mainly distributed along the ferrite grain boundaries. The WAAM high-strength steel displayed a higher volume fraction of austenite phase relative to its normal-strength counterpart, due to a higher content of carbon and other austenite stabilising elements (e.g. Ni and Mn), and a lower content of ferrite stabilisers (e.g. Si) [59].

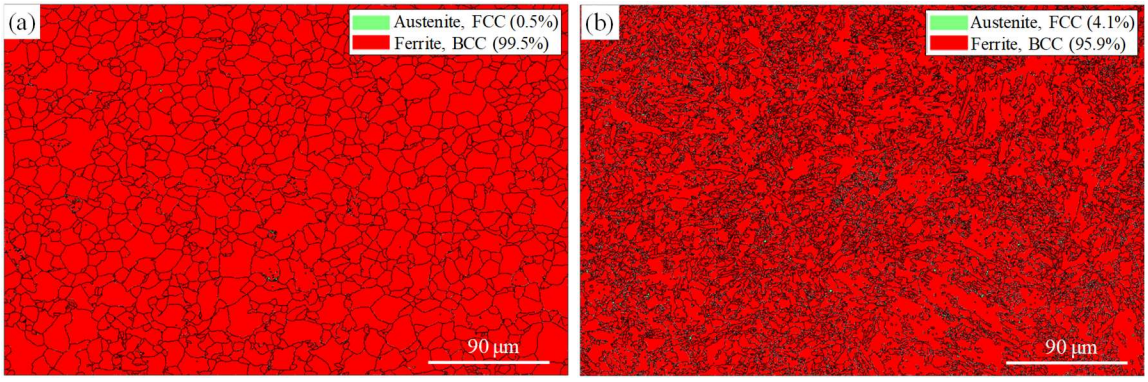


Fig. 40. Phase maps of WAAM (a) normal-strength steel and (b) high-strength steel.

5.3 Comparison with feedstock wire

In order to compare the microstructures of the parent feedstock wires and the WAAM materials, the cross-section and side face of the feedstock wires were examined using scanning electron microscopy (SEM). The SEM images of the cross-section and side face of the high-strength steel wire are illustrated in Fig. 41(a) and 41(b), respectively, and the {100}, {110} and {111} pole figures of the side face are presented in 41(c). The microstructure of the wire is shown to differ significantly, as expected due to the effects of the wire drawing process, from that of the

WAAM material, featuring fine, uniformly distributed grains in the cross-section, and a banded morphology in the microstructure of the side face. All the grains within the feedstock material are smaller than 1 μm, much finer than those within the WAAM material. The {111} pole figure exhibits a relatively intense crystallographic texture, with the grains elongated along the rolling direction, attributed to the plastic deformation experienced during the forming process.

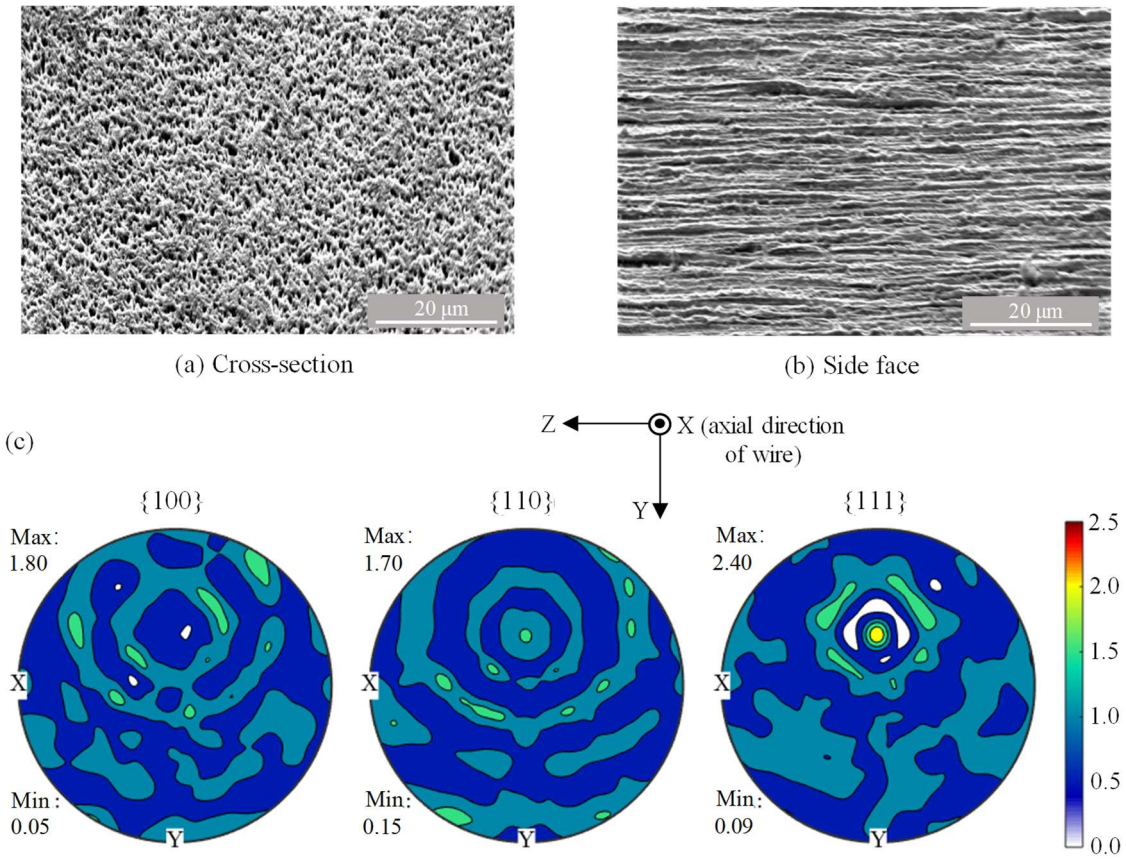


Fig. 41. SEM examination of high-strength steel wire: (a) SEM image of cross-section; (b) SEM image and (c) pole figures of side face.

6 Conclusions

A comprehensive experimental study into the mechanical properties and microstructure of WAAM plates made of ER70S-6 and ER110S-G steel wires has been presented. Tensile tests on a total of 137 coupons, covering different steel strengths, finishes, thicknesses, extraction directions and locations, and deposition strategies, have been conducted. 3D laser scanning and digital image correlation (DIC) were employed in the testing program to capture the geometric properties and deformation responses of the WAAM coupons, respectively. In parallel with the mechanical testing, microstructural characterisation of the WAAM steels has been performed through optical microscopy (OM) and electron backscatter diffraction (EBSD).

The tested WAAM coupons exhibited comparable Young's modulus values to that of conventional steels, and good ductility, with almost all satisfying the Eurocode 3 ductility requirements for hot-rolled steels. The WAAM process, however, resulted in the deposited material (excluding that close to the build plate) having lower strength compared to the values reported by manufacturer for conventional welds, with both the yield strength and ultimate strength being about 30% and 20% lower for the t_{nom} = 8 mm and 3 mm normal-strength steel coupons, respectively, and less than 5% lower for the t_{nom} = 3 mm high-strength steel coupons. The observed lower strengths are attributed to the slower cooling rates associated with the WAAM process, as reflected by the longer $t_{8/5}$ times. The machined coupons exhibited almost isotropic mechanical properties, while the geometric undulations of the as-built coupons led to a degree of anisotropy and some reduction in effective mechanical properties. No significant differences in tensile properties were observed with the employed deposition strategies, except for some variation in ductility.

According to the OM observations, the WAAM normal-strength steel plates exhibited a principally ferritic-pearlitic microstructure, while the WAAM high-strength steel plates displayed a mixed microstructure featuring ferrite, bainite and martensite. The EBSD analysis revealed a weak crystallographic texture for both the normal- and high-strength WAAM steels, which explained the observed mechanical properties being almost isotropic.

Data availability

The raw/processed data required to reproduce these findings cannot be shared at this time as the data also forms part of an ongoing study.

Acknowledgements

This research was possible thanks to funding and support from the European Union's Horizon 2020 research and innovation programme under grant agreement No. 820776 'Intelligent data-driven pipeline for the manufacturing of certified metal parts through Direct Energy Deposition process (INTEGRADDE).' The authors also gratefully acknowledge funding and support from the China Scholarship Council (CSC). Finally, the authors would like to thank Gordon Herbert and Les Clark for their contributions to the experimental study.

References

[1] ASTM (2017). Additive manufacturing - general principles - terminology. ISO/ASTM 52900.

[2] A. Paolini, S. Kollmannsberger, E. Rank, Additive manufacturing in construction: a review on processes, applications, and digital planning methods, Addit. Manuf. 30 (2019) 100894.

[3] W. Gao, Y. Zhang, D. Ramanujan, K. Ramani, Y. Chen, C.B. Williams, C.C. Wang, Y.C. Shin, S. Zhang, P.D. Zavattieri, The status, challenges, and future of additive manufacturing in engineering, CAD Comput. Aided Des. 69 (2015) 65–89.

[4] T.D. Ngo, A. Kashani, G. Imbalzano, K.T.Q. Nguyen, D. Hui, Additive manufacturing (3D printing): a review of materials, methods, applications and challenges, Compos. Part B. 143 (2018) 172–196.

[5] A. Kanyilmaz, A.G. Demir, M. Chierici, F. Berto, L. Gardner, S.Y. Kandukuri, P. Kassabian, T. Kinoshita, A. Laurenti, I. Paoletti, A. du Plessis, S.M.J. Razavi, Role of metal 3D printing to increase quality and resource-efficiency in the construction sector, Addit. Manuf. (2022) 102541.

[6] J. Ye, P. Kyvelou, F. Gilardi, H. Lu, M. Gilbert, L. Gardner, An end-to-end framework for the additive manufacture of optimised tubular structures, IEEE Access. 9 (2021) 165476-165489.

[7] C. Buchanan, L. Gardner, Metal 3D printing in construction: a review of methods, research, applications, opportunities and challenges, Eng. Struct. 180 (2019) 332–348.

[8] L. Gardner, P. Kyvelou, G. Herbert, C. Buchanan, Testing and initial verification of the world's first metal 3D printed bridge, J. Constr. Steel Res. 172 (2020) 106233.

[9] V.A. Silvestru, I. Ariza, J. Vienne, L. Michel, A.M. Aguilar Sanchez, U. Angst, R. Rust, F. Gramazio, M. Kohler, A. Taras, Performance under tensile loading of point-by-point wire and arc additively manufactured steel bars for structural components, Mater. Des. 205 (2021) 109740.

[10] T. Feucht, J. Lange, M. Erven, C.B. Costanzi, U. Knaack, B. Waldschmitt, Additive manufacturing by means of parametric robot programming, Constr. Robot. 4 (2020) 31–48.

[11] MX3D, Structural connector for TAKANAKA, 2019. < https://mx3d.com/industries/construction/connector-for-takenaka/ > [Accessed 28 May 2021]

[12] P. Kyvelou, H. Slack, D.D. Mountanou, M.A. Wadee, T.B. Britton, C. Buchanan, L. Gardner, Mechanical and microstructural testing of wire and arc additively manufactured sheet material, Mater. Des. 192 (2020) 108675.

[13] V. Laghi, M. Palermo, G. Gasparini, V.A. Girelli, T. Trombetti, On the influence of the geometrical irregularities in the mechanical response of wire-and-arc additively manufactured planar elements, J. Constr. Steel Res. 178 (2021) 106490.

[14] A. Ramalho, T.G. Santos, B. Bevans, Z. Smoqi, P. Rao, J.P. Oliveira, Effect of contaminations on the acoustic emissions during wire and arc additive manufacturing of 316L stainless steel, Addit. Manuf. 51 (2022) 102585.

[15] B. Wu, Z. Pan, D. Ding, D. Cuiuri, H. Li, J. Xu, J. Norrish, A review of the wire arc additive manufacturing of metals: properties, defects and quality improvement, J. Manuf. Process. 35 (2018) 127–139.

[16] F. Wang, S. Williams, P. Colegrove, A.A. Antonysamy, Microstructure and mechanical properties of wire and arc additive manufactured Ti-6Al-4V, Metall. Mater. Trans. A Phys. Metall. Mater. Sci. 44 (2013) 968–977.

[17] J. Gu, M. Gao, S. Yang, J. Bai, Y. Zhai, J. Ding, Microstructure, defects, and mechanical properties of wire + arc additively manufactured AlCu4.3-Mg1.5 alloy, Mater. Des. 186 (2020) 108357.

[18] Y. Zhai, P. Ma, The strengthening effect of inter-layer cold working and post-deposition heat treatment on the additively manufactured Al-6.3Cu alloy, Mater. Sci. Eng. A. 651 (2016) 18–26.

[19] T.A. Rodrigues, N. Bairrão, F.W.C. Farias, A. Shamsolhodaei, J. Shen, N. Zhou, E. Maawad, N. Schell, T.G. Santos, J.P. Oliveira, Steel-copper functionally graded material produced by twin-wire and arc additive manufacturing (T-WAAM), Mater. Des. 213 (2022) 110270.

[20] W.C. Ke, J.P. Oliveira, B.Q. Cong, S.S. Ao, Z.W. Qi, B. Peng, Z. Zeng, Multi-layer deposition mechanism in ultra high-frequency pulsed wire arc additive manufacturing (WAAM) of NiTi shape memory alloys, Addit. Manuf. 50 (2022) 102513.

[21] L. Sun, F. Jiang, R. Huang, D. Yuan, C. Guo, J. Wang, Anisotropic mechanical properties and deformation behavior of low-carbon high-strength steel component fabricated by wire and arc additive manufacturing, Mater. Sci. Eng. A. 787 (2020) 139514.

[22] Z. Lin, C. Goulas, W. Ya, M.J.M. Hermans, Microstructure and mechanical properties of medium carbon steel deposits obtained via wire and arc additive manufacturing using metal-cored wire, Metals. 9 (2019) 673.

[23] T.A. Rodrigues, V.R. Duarte, D. Tomás, J.A. Avila, J.D. Escobar, E. Rossinyol, N. Schell, T.G. Santos, J.P. Oliveira, In-situ strengthening of a high strength low alloy steel during Wire and Arc Additive Manufacturing (WAAM), Addit. Manuf. 34 (2020) 101200.

[24] A. Ermakova, A. Mehmanparast, S. Ganguly, J. Razavi, F. Berto, Investigation of mechanical and fracture properties of wire and arc additively manufactured low carbon steel components, Theor. Appl. Fract. Mech. 109 (2020) 102685.

[25] C.V. Haden, G. Zeng, F.M.C. Iii, C. Ruhl, B.A. Krick, D.G. Harlow, Wire and arc additive manufactured steel: tensile and wear properties, Addit. Manuf. 16 (2017) 115–123.

[26] T.A. Rodrigues, V. Duarte, J.A. Avila, T.G. Santos, R.M. Miranda, J.P. Oliveira, Wire and arc additive manufacturing of HSLA steel: effect of thermal cycles on microstructure and mechanical properties, Addit. Manuf. 27 (2019) 440–450.

[27] J. Ge, J. Lin, Y. Lei, H. Fu, Location-related thermal history, microstructure, and mechanical properties of arc additively manufactured 2Cr13 steel using cold metal transfer welding, Mater. Sci. Eng. A. 715 (2018) 144–153.

[28] E. Aldalur, F. Veiga, A. Suárez, J. Bilbao, A. Lamikiz, High deposition wire arc additive manufacturing of mild steel: strategies and heat input effect on microstructure and mechanical properties, J. Manuf. Process. 58 (2020) 615–626.

[29] C. Zhang, C. Shen, X. Hua, F. Li, Y. Zhang, Y. Zhu, Influence of wire-arc additive manufacturing path planning strategy on the residual stress status in one single buildup layer, Int. J. Adv. Manuf. Technol. 111 (2020) 797–806.

[30] CEN (European Committee for Standardization) (2016). Metallic materials - tensile testing - Part 1: method of test at room temperature. EN ISO 6892-1:2016.

[31] Geomagic Wrap 2017-3D Systems (Version 2017.0.2:64) [Software] Incorporated and its Licensors, 2017.

[32] Rhino 3D (Version 5 SR14 64-bit) 607 [Software] Robert McNeel & Associates, 2017.

[33] H. Hotelling, Analysis of a complex of statistical variables into principal components, J. Educ. Psychol. 24 (1933) 417–441.

[34] K. Pearson, LIII. On lines and planes of closest fit to systems of points in space, London, Edinburgh, Dublin Philos. Mag. J. Sci. 2 (1901) 559–572.

[35] P. Kyvelou, C. Huang, L. Gardner, C. Buchanan, Structural testing and design of wire arc metal additively manufactured square hollow sections, J. Struct. Eng. ASCE. 147 (2021) 04021218.

[36] Davis 10 (Version 10.1.1) [Software] La Vision GmbH, 2017.

[37] N. Hadjipantelis, B. Weber, C. Buchanan, L. Gardner, Description of anisotropic material response of wire and arc additively manufactured thin-walled stainless steel elements, Thin-Walled Struct. 171 (2022) 108634.

[38] X. Yun, L. Gardner, Stress-strain curves for hot-rolled steels, J. Constr. Steel Res. 133 (2017) 36–46.

[39] CEN (European Committee for Standardization) (2015). Eurocode 3 - design of steel structures - Part 1-1: general rules and rules for buildings. EN 1993-1-1:2005.

[40] CEN (European Committee for Standardization) (2017). Eurocode 3 - design of steel structures - Part 1-12: additional rules for the extention of EN 1993 up to steel grades S 700. EN 1993-1-12:2007.

[41] P.H. Mott, C.M. Roland, Limits to Poisson's ratio in isotropic materials, Phys. Rev. B - Condens. Matter Mater. Phys. 80 (2009) 1–4.

[42] J.P. Oliveira, T.G. Santos, R.M. Miranda, Revisiting fundamental welding concepts to improve additive manufacturing: from theory to practice, Prog. Mater. Sci. 107 (2020) 100590.

[43] P. Dirisu, S. Ganguly, A. Mehmanparast, F. Martina, S. Williams, Analysis of fracture toughness properties of wire + arc additive manufactured high strength low alloy structural steel components, Mater. Sci. Eng. A. 765 (2019) 138285.

[44] M. Mician, D. Harmaniak, F. Novy, J. Winczek, J. Moravec, L. Trško, S960MC steel in the HAZ of welded joints evaluated, Metals. 10 (2020) 18.

[45] E. Keehan, J. Zachrisson, L. Karlsson, Influence of cooling rate on microstructure and properties of high strength steel weld metal, Sci. Technol. Weld. Join. 15 (2010) 233–238.

[46] British Standards Institution (2001). Welding - recommendations for welding of metallic materials - Part 2: arc welding of ferritic steels. BS EN 1011-2:2001.

[47] N. Kozamernik, D. Bračun, D. Klobčar, WAAM system with interpass temperature control and forced cooling for near-net-shape printing of small metal components, Int. J. Adv. Manuf. Technol. 110 (2020) 1955–1968.

[48] ASTM (2017). Standard guide for preparation of metallographic specimens. ASTM E3-11:2017.

[49] N. Brodusch, H. Demers, R. Gauvin, Imaging with a commercial electron backscatter diffraction (EBSD) camera in a scanning electron microscope: a review, J. Imaging. 4 (2018) 88.

[50] Esprit (version 2.3) [Software] Bruker, 2020.

[51] ImageJ (version 1.8.0) [Software] National Institutes of Health, 2015.

907 [52] M. Rafieazad, M. Ghaffari, A. Vahedi Nemani, A. Nasiri, Microstructural evolution and
908 mechanical properties of a low-carbon low-alloy steel produced by wire arc additive
909 manufacturing, Int. J. Adv. Manuf. Technol. 105 (2019) 2121–2134.

910 [53] D.S. Mai, Q.H. Hoang, A study on wire and arc additive manufacturing of low-carbon steel
911 components: process stability, microstructural and mechanical properties, J. Brazilian Soc.
912 Mech. Sci. Eng. 42 (2020) 1–11.

913 [54] N. Hansen, Boundary strengthening over five length scales, Adv. Eng. Mater. 7 (2005) 815–
914 821.

915 [55] R.W. Armstrong, The (cleavage) strength of pre-cracked polycrystals, Eng. Fract. Mech. 28
916 (1987) 529–538.

917 [56] Z. Yu, T. Yuan, M. Xu, H. Zhang, X. Jiang, S. Chen, Microstructure and mechanical properties
918 of Al-Zn-Mg-Cu alloy fabricated by wire + arc additive manufacturing, J. Manuf. Process. 62
919 (2021) 430–439.

920 [57] Y.L. Dai, S.F. Yu, A.G. Huang, Y.S. Shi, Microstructure and mechanical properties of high-
921 strength low alloy steel by wire and arc additive manufacturing, Int. J. Miner. Metall. Mater. 27
922 (2020) 933–942.

923 [58] F.J. Humphreys, Grain and subgrain characterisation by electron backscatter diffraction, J.
924 Mater. Sci. 36 (2001) 3833–3854.

925 [59] A. Vahedi Nemani, M. Ghaffari, A. Nasiri, Comparison of microstructural characteristics and
926 mechanical properties of shipbuilding steel plates fabricated by conventional rolling versus wire
927 arc additive manufacturing, Addit. Manuf. 32 (2020) 101086.

928 [60] V. Laghi, M. Palermo, L. Tonelli, G. Gasparini, L. Ceschini, T. Trombetti, Tensile properties
929 and microstructural features of 304L austenitic stainless steel produced by wire-and-arc additive
930 manufacturing, Int. J. Adv. Manuf. Technol. 106 (2020) 3693–3705.

931